An evaluation of the regional distribution and wet deposition of secondary inorganic aerosols and their gaseous precursors in IFS-COMPO preparatory to cycle 49R1.

Jason E. Williams [1], Swen Metzger [2], Samuel Rémy [3], Vincent Huijnen [1] and Johannes Flemming [4]

1 R&D Weather and Climate Modeling, Royal Netherlands Meteorological Institute, De Bilt, the Netherlands

2 ResearchConcepts io GmbH, Freiburg, Germany

3 HYGEOS, Lille, France

4 European Centre for Medium-Range Weather Forecasts, Bonn, Germany

Abstract

Secondary Inorganic Aerosol (SIA) makes up a considerable fraction of the total particulate matter exposure and, thus, is an important product from any forecasting system of atmospheric composition and air quality. The subsequent loss to the surface of SIA via dry and wet deposition determines the duration of the exposure time for humans and the extent of acidification imposed on sensitive ecosystems. Here we provide a description and evaluation of the most recent updates made towards aerosol production, aerosol scavenging and wet deposition components of the global Integrated Forecast System-COMPOsition (IFS-COMPO) chemical forecasting system, which is used as part of the Copernicus Atmosphere Monitoring Service. The implementation of the EQSAM4Clim simplified thermodynamic module in IFS-COMPO, for use in cycle 49R1, changes the efficacy of phase transfer of SIA precursor gases (sulphur dioxide, nitric acid and ammonia) which significantly impacts the respective SIA particulate concentrations by changing the fraction converted into SIA. Comparisons made against observational composites at the surface for Europe, the U.S., and Southeast Asia during 2018 show reductions in the global yearly mean bias statistics for both sulphates and nitrates. Updating the IFS-COMPO model towards cycle 49r1 increases both the burden and lifetime of sulphate and ammonium particles by one third. Coupling EQSAM4Clim into IFS-COMPO provides a better description of the partitioning between state phases involving ammonia and ammonium across regions, whereas changes for sulphate are minimal. For nitric acid and nitrates, the partitioning changes significantly, leading to lower particulate concentrations and a corresponding increase in gas-phase nitric acid with an associated improvement in surface nitrate. There is also a shift in the particle size distribution, with less nitrate production in the coarse mode and more in the fine mode. The impact on the total regional wet deposition values is generally positive, except for sulphates in the U.S. and ammonium particles in Southeast Asia which are strongly influenced by the precursor emission estimates. This provides confidence that this update to IFS-COMPO has the ability to provide accurate deposition fluxes of S and N at global scale.

1 Introduction

Secondary Inorganic Aerosol (SIA) is found throughout the troposphere, where resident concentrations are dependent on Temperature (T), Relative Humidity (RH) and concentrations of inorganic precursor gases, namely water vapour (H_2O), sulphur dioxide (SO_2), ammonia (NH_3) and nitric acid (HNO_3). High concentrations of SIA contribute to total Particulate Matter that are smaller than using various predefined particle sizes namely: 1.0μm (PM1.0), 2.5μm (PM2.5) and 10μm (PM10) (Liu et al, 2022), and have detrimental effects on both human health and visibility (Sharma et al, 2020; Ting et al., 2021). The main types of SIA are ammonium sulphate (($NH_4)_2SO_4$), ammonium bisulphate (NH_4HSO_4) and ammonium nitrate (NH_4NO_3). Once formed, the sulphates are very stable and deposit to the surface, whereas NH_4NO_3 is more unstable and can decompose back to the precursor gases (Feick and Hainer, 1954) depending on T and RH. These particles can be transported out of source regions subsequently influencing air quality in neighbouring countries (e.g., Vieno et al., 2014; Chang et al., 2022). Anthropogenic activity makes a significant contribution to SIA formation via the emission of NO_x (oxidised nitrogen in the form of NO and NO_2), NH_x (reduced nitrogen) and SO_2, where there has been a general trend of decreasing sulphur (S) and nitrogen (N) emissions in the EU, U.S. and China (Tørseth et al., 2012; Aas et al., 2019; Benish et al., 2022; Jiang et al., 2022) resulting in an increasing fraction of SIA consists of NH_4NO_3. This results in a decrease in the lifetime of SIA, due to the increased instability of NH_4NO_3 due to variations in RH and temperature (e.g. Williams et al., 2015; Metzger et al., 2002; 2006), reducing the potential for reduced long-range transport out of the source regions (He et al., 2018).

At RH values above 50%, SIA take up water and exist in a deliquescent state. At high RH values of 80-100%, SIA formation is enhanced (Gao et al., 2020) therefore, under constant or changing emissions, SIA is likely to become more ubiquitous in a warming atmosphere. The hygroscopic growth of SIA alters both the optical properties (in terms of scattering and absorption) and interactions with gas-phase trace species via changes in pH (e.g. Jayne et al., 1990; Shi et al, 2018). The concentrated salt solution produced typically has higher ionic strength than cloud droplets with pH values ranging between -1 to 6 (Ault, 2020). The high solubility of SIA results in the scavenging into aquated aerosols and clouds being a dominant loss term. This has impacts in terms of the acidification of sensitive ecosystems and an increase in eutrophication due to high nitrogen loading in inland water bodies, which can result in the exceedance of critical loads for vegetation (e.g. Sun et al., 2020). The uptake of carbon to land is also enhanced with an increase in N loading (Holland et al., 1997; Reary et al., 2008). Once dissolved in solution, SIA dissociates efficiently into the respective ionic constituents (e.g. nitrate (NO_3^-), ammonium (NH_4^+) and sulphate ($SO_4^=$)) whereas these anions/cations are deposited on land during precipitation events.

A distinct difference exists with respect to the main source terms for the various SIA species. For NO_x and NH_x species, particle formation is sensitive to the resident gas-phase precursor species, temperature, and RH, in the absence of aqueous phase droplets. For SO_4^{2-}, production occurs almost exclusively in the aqueous phase after SO_2 is scavenged into cloud and fog, whose overall oxidation rate is dependent on the prescribed pH in solution. Recent studies have shown that the correct prescription of cloud pH is necessary to account for changes in SO_4^{2-} efficacy over long time scales for the determination of long-term trends with respect to resident concentrations (Thurock et al., 2019; Myriokefalitakis et al., 2022). The representation of acidity in tropospheric aerosols and clouds ranges significantly across large-scale atmospheric models. The most simplistic representation is to use a fixed cloud water pH of between 5.0-5.6, thus effectively representing the impact of dissolved carbon dioxide (CO_2). A more accurate representation includes the influence of other dissolved species which either acidify (e.g. HNO_3, H_2SO_4) or buffer (e.g. NH_3) the pH of the solution once scavenged via irreversible uptake. This is the approach adopted in the Integrated Forecasting System with atmospheric composition extension (IFS-COMPO) for both cloud and precipitation. Other SO_4^{2-} production terms involving e.g. methyl-hydroperoxide (CH_3OOH) have been shown to be of secondary importance towards the total SO_4^{2-} production (Myriokefalitakis et al., 2022). The more buffering of solution due to the scavenging and dissolution of NH_3, the faster the conversion rate as dictated by the rate of reaction of HSO_3^- being less than that for $SO_3^=$ (Warneck, 1991).

One dominant loss term for SIA is wet deposition in precipitation to the surface. Previous global tropospheric modelling studies have been performed focusing on the temporal accuracy and yearly deposition totals at continental scale for NH_x and SO_x (Zhang et al., 2012; Kanikadou et al., 2016; Ge et al., 2021), as well as multi-model intercomparison studies to examine the variability across different models and the main assumptions causing such differences (Dentener et al., 2006; Bain et al., 2017; Tan et al., 2018). The accuracy of any model towards capturing the correct wet deposition terms is a balance between the accuracy of the precursor emission inventory, the distribution of the cloud liquid water content (defining the cloud Surface Area Density, SAD), the representation of the formation and distribution of aerosol particles, the extent of phase-transfer and the parametrizations adopted for describing dry/wet deposition to the surface.

The IFS-COMPO model is a large-scale global model used for operational analyses and air quality forecasts (Rémy et al., 2024) used in the Copernicus Atmosphere Monitoring Service (CAMS; Peuch et al. 2022). This service provides forecasts and reanalysis of trace gases and aerosols for the purpose of informing national service providers and policy makers. It currently provides chemical/aerosol forecast products, among them Ozone (O_3), Nitrogen Dioxide (NO_2), SO_2, PM2.5, PM10 and Aerosol Optical Depth. One focus of the recent updates made to IFS-COMPO was the reduction of biases and increase in correlation for aerosol products against observations (Rémy et al., 2024). Reduced and oxidised nitrogen deposition can also be future CAMS products which will benefit from the improved speciation between gaseous and particulate nitrogen.

In this paper we present an analysis of the regional performance of IFS-COMPO Cy48r1 and the version used for developing Cy49r1 (hereafter referred to as pre-cy49r1) towards the surface distributions N and S gaseous precursors for SIA and the associated particle concentrations and distributions as evaluated against ground based observation networks, with special focus on the application of latest update of EQSAM4Clim (Metzger et al., 2024) in the global chemical forecasting model IFS-COMPO pre-Cy49r1. This work is both parallel and complementary to the recent evaluation of the performance of IFS-COMPO Cy48r1 and pre-Cy49r1 with respect to regional PM2.5 distributions and Aerosol Optical Depth presented in Rémy et al (2024). The influence on regional wet and dry deposition terms is subsequently evaluated to assess the application of both EQSAM4Clim (Metzger et al, 2024) and the deposition schemes. In Sect. 2 we provide details of the IFS-COMPO simulations used, a brief description of the latest model updates and emissions used. In Sect 3 we describe the observational networks against which the surface evaluations are performed for the precursor gases and resulting SIA particulates. In Sect. 4 we provide details of the changes in regional surface concentrations of precursor gases and associated particulates and regional yearly mean statistics and in Sect 5., we compare the yearly mean wet deposition fluxes against observations for Europe, the U.S. and Southeast Asia and discuss improvements. Finally, in Sect. 6 we present some further discussion and conclusions from our study. Additional information in support of the main findings is also given in the supplementary material.

2 General information on the most recent IFS-COMPO versions

The IFS-COMPO global composition model (previously known as C-IFS) is used for operational air quality analyses and forecasts as part of CAMS. The modelling and data assimilation framework is regularly updated. During 2023 IFS-COMPO was based on the Cy48r1 version of IFS (https://www.ecmwf.int/en/elibrary/81374-ifs-documentation-cy48r1-part-viii-atmospheric-composition ; last access: 20 February 2024)), Since end of 2024, IFS-COMPO has moved to the pre-Cy49r1 version. IFS-COMPO pre-Cy49r1 has been shown to improve on the evaluated biases simulated in previous cycles for key products such as O_3 and NO_2 (https://atmosphere.copernicus.eu/eqa-reports-global-services ,last access 17 February 2025). Several updates were introduced in Cy49r1 to improve the aerosol component, the description of wet deposition and the representation of pH in clouds and aerosols. These include the application of the EQSAM4Clim approach and other developments associated with cloud scavenging (Metzger et al, 2016; Metzger et al., 2024; Rémy et al, 2024). For brevity, we only provide a brief description of the updates in Cy49r1 relevant to this study. Further details are available in Rémy et al. (2024), which also includes a schematic representation of the model

2.1 Updates in IFS-COMPO in pre-Cy49r1

IFS-COMPO Pre-Cy49r1 is built on the previous operational cycle (Cy48r1) and contains 8 distinct aerosol types with multiple bins for size segregation, namely sea salt, desert dust, organic carbon, black carbon, $SO_4^=$, fine and coarse NO_3^-, NH_4^+ and Secondary Organic Aerosol. For pre-Cy49r1 updates have been made to the aerosol component of the model in the form of modifying both the description and properties of desert dust and sea-salt, the aging of Carbonaceous aerosol and an update to the aerosol optics by changing the assumptions used for the $SO_4^=$ aerosol when referencing the lookup table for Mie scattering. This impacts the resident lifetimes, radiative properties and the long-range transport for each of the aerosol species. The modifications to the description of the aerosol optics have been shown to improve the simulation of Aerosol Optical Depth (AOD) and Ångström exponent when compared against regional observations (Rémy et al., 2024). The gas-phase chemistry, photolysis and dry deposition are identical to that used in Rémy et al. (2024) and as described in Williams et al. (2022). For brevity, and that this study is only concerned with soluble aerosols, we refer the reader to Rémy et al. (2024) for more explicit details related to the other aerosol types.

For pre-Cy49r1 there has been an integration of the aerosol and chemistry components in the code to make them more consistent, where both the sulfur and nitrogen cycles are now represented through the aerosol module (for particulate species) and the chemistry module (for gaseous species and aqueous $SO_4^=$ production). The aerosol module also provides additional input to the chemistry module to better represent heterogeneous reactions (via

153   Surface Area Density (SAD)) and the effects of aerosols on photolysis rates. The extent of gas–particle partitioning
154   and conversion via heterogeneous reactions on dust and sea-salt particles are outlined in Rémy et al. (2019), as
155   based on the work of Hauglustaine et al. (2014). In Cy48r1, the first version of the EQuilibrium Simplified Aerosol
156   Model (EQSAM; Metzger et al., 2002) was implemented for the calculation of e.g. NH_4NO_3 concentrations. These
157   parameterizations rely on meteorological data provided by IFS, as well as gaseous precursors such as HNO_3 and
158   NH_3 from the chemistry module. The gas–particle partitioning scheme estimates compound production through
159   the neutralization of HNO_3 by NH_3 left over after the neutralization of H_2SO_4. It also accounts for the formation
160   of specific compounds from heterogeneous reactions of HNO_3 with calcite (found in dust aerosol) and sea-salt
161   particles.

162   In IFS-COMPO pre-Cy49r1, EQSAM4Clim is used to estimate the gas/particle partitioning of the HNO_3-NO_3^- and
163   NH_3-NH_4^+ couples and to provide an estimate of the aerosol pH. The pH of aqueous solutions, aquated aerosols
164   and precipitation is now updated each time-step using the EQSAM4Clim approach accounting for additional
165   cations (Ca^{2+}, Mg^{2+}, Na^+, K^+), anions ($SO_4^=$, HSO_4^-, NO_3^-, Cl^-) and their solute interactions, whose methodology
166   is comprehensively described in Metzger et al. (2012, 2016, 2024). This replaces the original estimate of the pH
167   of the solution determined by summing the contributions from dissolved CO_2 and strong acids (HNO_3, HSO_3^-,
168   H_2SO_4, NO_3^- and Methane Sulfonic Acid) which is buffered by dissolved NH_3. The contribution towards the pH
169   of the solution of dissolved Formic and Acetic acid (HCOOH and CH_3COOH, respectively) are also now
170   accounted for in pre-Cy49r1, which has been shown to contribute to the pH in cloud droplets (Shah et al., 2020).
171   This impacts the phase-transfer, speciation, and subsequent aqueous-phase oxidation of SO_2 in cloud droplets (thus
172   impacting $SO_4^=$). Also, the loss of gas-phase species such as e.g. H_2O_2 and the corresponding formation of SIA
173   particles is affected. Note that both the original (Cy48r1) and updated (pre-Cy49r1) approaches account for the
174   most dominant gaseous contributions towards the pH of the solution, namely SO_2, HNO_3 and NH_3. This means
175   that differences imposed in cloud pH are naturally less than the associated changes in aerosol pH. The aqueous
176   phase oxidation of SO_2 by transition metal ions (Fe^{2+}, Mg^{2+}) is not currently accounted for but considered a minor
177   pathway.

178   Below cloud scavenging of gaseous precursors is also affected by the pH of solution (e.g. Seinfeld and Pandis,
179   2006). In Cy48r1 fixed values for cloud pH are used over land (pH=5.0) and ocean (pH=5.6), thus only providing
180   limited variability with respect to regions affected by both high and low emissions. In pre-Cy49r1 this has been
181   updated such that the calculator of the pH is coupled to resident trace gas and aerosol concentrations to improve
182   consistency within IFS-COMPO and to provide variable scavenging rates dependent on tropospheric composition.

183   In Cy48r1, the wet deposition routines for aerosols and chemistry in IFS-COMPO are distinct, though both utilise
184   a scheme adapted from Luo et al. (2019). To ensure a consistent approach between aerosol and trace gases wet
185   deposition, and to simplify code maintenance, these separate implementations have been merged into a unified
186   routine. This new routine now represents the wet deposition processes for both aerosols and chemical species and
187   is called with either chemical or aerosol tracers as input. As with Cy48r1 and previous versions, the wet deposition
188   routine in pre-Cy49r1 is executed twice: once for large-scale precipitation and once for convective precipitation.
189   In the case of convective precipitation, the assumed precipitation fraction has been standardised to 0.05 (whereas
190   in Cy48r1 a value of 0.1 was used for chemistry scavenging and 0.05 for aerosol scavenging).

191   Additional upgrades have been made for aerosol wet deposition as follows: (i) The aerosol activation
192   parameterization of Verheggen et al. (2007) has been implemented. This parameterization estimates the fraction
193   of aerosols that can be scavenged through in-cloud processes as a function of temperature. It is applied to mixed
194   clouds, specifically for temperatures between the freezing point and 233K. For temperatures above 0°C, the
195   consistency of the parameters determining the fraction of aerosols subject to in-cloud wet deposition with the
196   results of the Verheggen parameterization has been verified. (ii) For below-cloud scavenging of aerosol species,
197   the scavenging rates have been updated to reflect the particle size dependency more accurately as described by
198   Croft et al. (2009). This update includes adjustments to the below-cloud scavenging parameters, which describe
199   the efficiency with which aerosols are removed by rain and snow, depending on the species and the assumed size
200   distribution.

201   **2.2 Setup of model simulations**

202   The IFS-COMPO simulations used for evaluating the impact of IFS-COMPO atmospheric composition upgrades
203   proposed for pre-Cy49r1 on tropospheric composition, precursor gases, particle distributions and wet deposition
204   terms employ both the IFS cycles Cy48r1 and pre-Cy49r1. Here, pre-Cy49r1 denotes the IFS-COMPO Cy48r1
205   including updates of aerosol/chemistry modules which are now applied in IFS pre-Cy49r1. The meteorological
206   component is the same between simulations and corresponds to Cy48r1. Still, marginal differences may occur

207 between simulations due to a coupling of gases and aerosol with radiation, which is active by default. The
208 simulations presented here are for the year 2018, with a one-month spin-up period. The vertical resolution uses
209 137 individual model levels and a horizontal resolution of T_L511, corresponding to approx. 0.4° x 0.4° (with further
210 details being given at https://confluence.ecmwf.int/display/UDOC/L137+model+level+definitions). The
211 experiments do not include the data assimilation of observations, meaning that although the changes shown will
212 not be directly visible in the final operational forecast, they will influence the resulting skill scores for e.g. PM2.5.
213 Meteorology is initialised every 24 hours based on ERA5 reanalysis data, i.e. IFS-COMPO is run in a cyclic
214 forecast mode. A 15-minute chemical time-step is used for solving a modified version of CB05 tropospheric
215 chemistry (Williams et al., 2022), excluding active stratospheric chemistry for efficiency (with this study being
216 focused on changes at the surface). Three-hourly 3D global output is used for the analysis and aggregated into
217 weekly, monthly, and yearly mean values.

218 The details of the experiments are summarised in Table 1. The Cy48r1 reference simulation pertains to the 48R1
219 version of IFS-COMPO while the pre-Cy49r1 simulation is based on the version described in Rémy et al (2024),
220 which is Cy48r1 updated with new components for use in future versions of IFS-COMPO. The pre-
221 Cy49r1_NOEQ4C simulation is identical to the pre-Cy49r1 simulation, except the EQSAM4Clim module
222 (Metzger et al., 2024) is deactivated. For future reference, the experiment identities on the ECMWF Multiversion
223 Asynchronous Replicated Storage system (MARS) are hylm (Cy48r1), i3bw (pre-Cy49r1_NOE4C) and i3ad (pre-
224 Cy49r1). These three simulations use a configuration, and emissions as those used for the simulations presented
225 in Rémy et al. (2024) for evaluating PM. We select the year 2018 to provide further evaluation which is
226 complimentary to the results presented for 2019 in Rémy et al. (2024).

227 **Table 1:** Definitions of the IFS-COMPO simulations used in this study. The experiment ID's can be used to
228 retrieve the original data from the MARS archiving system hosted at ECMWF.

Simulation	Experiment ID	Comments
Cy48r1	rd.hylm	Reference Cy48r1 model version
pre-cy49r1_NOEQ4C	rd.i3bw	As Cy48r1 but with all composition modeling updates for pre-cy49r1, except EQSAM4Clim.
pre-cy49r1	rd.i3ad	As Cy48r1, but with all composition modeling updates for pre-cy49r1, particularly activating EQSAM4Clim in both aerosols and cloud droplets

229

230 The anthropogenic emissions adopted in these configurations are taken from CAMS_GLOB_ANT v5.3 (Soulie et
231 al., 2024), biogenic emissions taken from the CAMS_GLOB_BIO v3.1 dataset (Sindelarova et al., 2022;
232 http://eccad.aeris-data.fr/) and biomass burning emissions taken from GFAS v1.2 (Kaiser et al., 2012). All
233 emissions are provided at 0.1 x 0.1 resolution at a monthly frequency, except for the biomass burning emissions
234 which are prescribed daily. For biomass burning and anthropogenic emissions from specific sectors vertical
235 profiles are used representing pyrogenic convection or industrial stack heights, with other emissions being applied
236 in the lowest model level. A diurnal cycle is imposed for isoprene and biomass burning emissions to capture either
237 photolytic activity or the tropical burning cycle. Volcanic outgassing of SO_2 is also included based on Andres and
238 Kasgnoc (1998). For di-methyl sulphide (DMS) oceanic emissions are based on Kloster et al. (2006) i.e. not
239 coupled to sea surface temperature which controls biogenic activity (Deschaseaux et al., 2019). Moreover, direct
240 production of $SO_4^=$ and HNO_3 in hot shipping exhausts is not accounted for (e.g. von Glasow et al., 2003).

241 **3 Observations**

242 For $SO_2(g)/SO_4^{2-}$, $NH_3(g)/NH_4^+$ and $HNO_3(g)/NO_3^-$ evaluation in Europe we compare IFS-COMPO model output
243 against data taken from the EMEP measurement network as stored on the EBAS data archive (EMEP, Torseth et
244 al., 2012; https://ebas.nilu.no/; last access 6 June 2025) using a composite of 49 individual stations located in 10
245 different countries, as shown in the top panel of Fig A1 in the Appendix. We chose sites which monitor both the
246 pre-cursor gases and associated SIA simultaneously to ensure valid comparisons. The sampling sites are located
247 mostly in northern and eastern Europe, but co-location of model output means the comparison is still valid., albeit
248 having less representation for southern Europe. For the U.S. we compare model output aggregated on a weekly

249 basis against data provided at locations included in the Clean Air Status and Trends Network (CASTNET;
250 https://www.epa.gov/castnet, last access: 6 June 2025) using a composite of 92 individual stations distributed
251 across the U.S. . The distribution of the U.S. measurement sites is shown in the middle panel of Fig. A1 in the
252 Appendix. For $NH_3(g)$ not direct measurements are available from the CASTNET database, therefore we compare
253 against both weekly and yearly mean values as derived from sites located near CASTNET stations (within 0.5
254 degrees radius) i.e. 92 of the current 106 sites in the Ammonia Monitoring Network (AMoN,
255 https://nadp.slh.wisc.edu/networks/ammonia-monitoring-network/ , last access on 6 June 2025). No filtering has
256 been applied to any of the observational data used in this study. Unfortunately conducting a similar analysis in
257 Southeast Asia was not possible owing to the unavailability of both precursor and SIA weekly measurements.

258 For evaluating the SIA particle concentrations, we use available data from the EMEP (Europe), CASTNET (US)
259 and the Acid Deposition Monitoring Network in East Asia (EANET, https://www.eanet.asia/ , last access: 6 June
260 2025; S. E. Asia) for SO_4^{2-}, NH_4^+ and NO_3^-. The EANET network includes 41 individual stations covering a wide
261 region, whose location is shown in the bottom panel of Fig A1 in the Appendix. Although we use all the
262 observations provided in each database, the distribution is non-homogeneous, with those in EMEP being clustered
263 towards northern Europe and those in Southeast Asia spanning a large area from eastern China to Japan. The
264 locations of the stations used for evaluation are also shown (black circles) on the corresponding figures associated
265 with regional and spatial validation.

266 For the wet deposition totals we use data taken from the same measurement networks and sampling frequency as
267 those used for evaluating the gaseous precursors and SIA (EMEP, CASTNET, EANET) thus removing any
268 differences potentially introduced by spatial sampling which would complicate the comparisons discussed here.
269 Although seasonal variability is of interest, the EANET wet deposition totals are only provided as yearly mean
270 values placing constraints on the sampling frequency used for the analysis. Therefore, the averaging period chosen
271 for the evaluation is constrained by the frequency and availability of the data from Southeast Asia. All statistical
272 metrics represent spatio-temporal averages unless otherwise noted, combining all station-time pairings into a single
273 evaluation vector per region and species. No filtering of the data was performed before making the comparisons.

4 The influence of pH on SIA chemical precursors and particulates

275 The efficacy of SIA formation is strongly governed by the resident concentrations of the gaseous precursors.
276 Therefore, changes imposed with respect to the parameterizations used for simulating particle formation also have
277 an associated feedback effect on the precursors, due to changes in the fractional uptake governed by the solute pH.
278 In this section, we evaluate the temporal and regional distribution and biases of both gaseous precursors (SO_2,
279 NH_3, HNO_3) and associated SIA (namely $SO_4^=$, NH_4^+, NO_3^-) simulated by IFS-COMPO for Europe, the U.S. and
280 Southeast Asia. Mixing ratios and particle concentrations are strongly influenced by the description and
281 distribution of the primary emission sources, meteorology, dry/wet deposition, aerosol pH (for NH_x and NO_x) and
282 atmospheric transport. To investigate the ability of IFS-COMPO towards capturing the observed distributions, we
283 compare both weekly and yearly mean composites for Cy48r1 and pre-Cy49r1 against the corresponding values
284 derived from in-situ measurements.

4.1 SO_2 and $SO_4^=$

286 Figure 1 shows the regional monthly mean distributions in surface SO_2 mixing ratios for July and December 2018
287 for Cy48r1, along with the relative percentage differences between Cy48r1, pre-Cy49r1_NOEQ4C and pre-
288 Cy49r1. When comparing the spatial distributions across regions, Europe exhibits the lowest SO_2 mixing ratios in
289 Cy48r1, where the region has undergone strong mitigation practices over the last decades (e.g. Vestreng et al,
290 2007). The maps for July show higher mixing ratios towards the east, with a significant contribution from shipping
291 in the Mediterranean and the English Channel. For December, the highest mixing ratios occur over the continent,
292 most notably in Germany and Poland. For the US, a stark east-west gradient exists as governed by the continental
293 distribution in anthropogenic emissions, with higher emissions towards the East Coast, again with a seasonal
294 signature. Maximal surface mixing ratios are 5-10 times higher than those simulated for Europe distributed over a
295 much larger area. As expected, China exhibits the highest regional mixing ratios of between 10-20 ppb over the
296 entire country, which is approximately 20 times higher than those simulated for Europe for both months shown.

297 When comparing Cy48r1 against pre-Cy49r1_NOE4C there are reductions in $[SO_2(g)]$ at the surface for all regions
298 of between 0-10%, resulting in limited increases in SO_4^{2-} production of a few percent due to changes other than
299 those related to the application of EQSAM4Clim. This small increase in the SO_4^{2-} production is reversed when

300 applying the EQSAM4Clim pH methodology (Metzger et al., 2024), where the conversion efficacy of SO_2 is faster
301 at a more alkalinic pH. Table 2 provides the global budget terms for $SO_2(g)$, which shows that in addition to
302 primary emission, approximately one third of SO_2 in the troposphere comes from the oxidation of DMS by the
303 hydroxyl radical (OH), with DMS originating from biogenic activity in the oceans.

304 In Cy48r1, approximately 20% of SO_2 is oxidised in the gas-phase and 43% in the aqueous phase, with the
305 remaining 37% being lost to surface via dry and wet deposition. This increase in gas-phase production via OH is
306 linked to changes imposed by differences in O_3-NO_x reaction cycles near anthropogenic source regions which
307 results in a small increase in O_3 of a few percent (not shown). The corresponding values for pre-Cy49r1_NOE4C
308 show changes in the order of a few percent across terms, increasing the global burden by of $SO_2(g)$ by 1.4% mostly
309 in the lower troposphere. For pre-Cy49r1 the application of EQSAM4Clim pH in cloud droplets reduces both the
310 uptake and oxidation of SO_2 by reducing aquated sulphite ($[SO_3^{2-}]_{aq}$, $pKa(HSO_3^-)$ =7.2) and an enhancement of the
311 gas-phase oxidation due to increased OH, resulting in more gas-phase production of H_2SO4. This is subsequently
312 scavenged into solution further increasing solution acidity (lowering pH values) in case of excess SO_4^{2-}
313 (insufficient cations to completely neutralise all SO_4^{2-}).

314 Figure 2 shows a comparison of weekly $[SO_2(g)]$ and $[SO_4^{2-}]$ surface composites as simulated in IFS-COMPO
315 against weekly composites of measurements taken from the EMEP measurement network (top left panel). For
316 $SO_2(g)$ a consistent positive bias exists for the entire year across all IFS-COMPO simulations suggesting emission
317 estimates which are high. Surface concentrations exhibit around 100% positive bias, increasing to almost 200%
318 during wintertime. The variability in the observational means (grey shaded area) does indicate that the simulated
319 increase in surface $[SO_2(g)]$ during wintertime does occur at some of the measurement sites. The corresponding
320 observational means of $[SO_4^{2-}]$ show that there is higher weekly variability during wintertime than summertime,
321 with concentrations ranging typically between 1.0-2.0 $\mu g/m^3$. This significant wintertime weekly variability is
322 simulated well by IFS-COMPO across all simulations, where both Cy48r1 and pre-Cy49r1 exhibit significant
323 positive biases of 0.5-1.0 $\mu g/m^3$. Surprisingly, pre-Cy49r1_NOE4C has the lowest bias during wintertime of
324 around 0.2-0.5 $\mu g/m^3$. For pre-Cy49r1, there is an increase in surface $[SO_4^{2-}]$ by approximately 10-25%., albeit
325 with a significant negative bias of around 0.8-1.5 $\mu g/m^3$. During summertime, the weekly variability in the
326 observed weekly means is insignificant. All simulations capture this limited variability, with differences across
327 simulations being around 0.1-0.2 $\mu g/m^3$. Due to the primary source term of SO_2 being direct emissions, the high

328 [SO_2(g)] simulated for Eastern Europe suggests a local overestimate (c.f. Fig. 1).
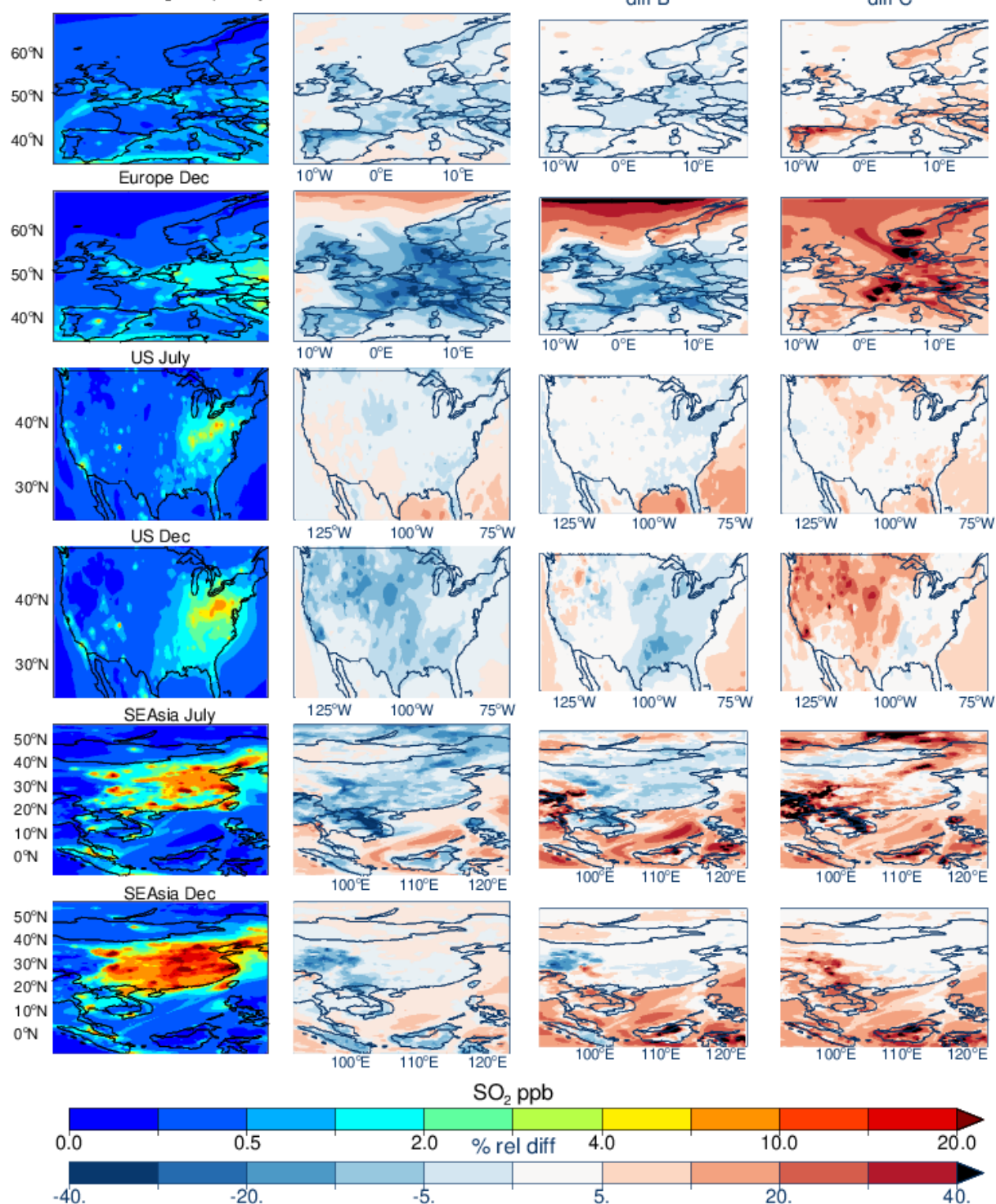
329

330 **Figure 1:** The horizontal monthly mean distribution for surface SO_2 for Cy48r1 for July and December 2018 for
331 Europe (top), the United States (middle) and Southeast Asia (bottom). The corresponding relative differences
332 when compared against the other simulations. Panel definitions: Diff A= (pre-cy49r1_NOEQ4C-Cy48r1)/Cy48r1;
333 Diff B=(pre-cy49r1-Cy48r1)/Cy48r1 and Diff C=(pre-Cy49r1-pre-Cy49r1_NOEQ4C)/Cy48r1.

334

335 **Table 2** The tropospheric SO_2 budget in Tg S/year for 2018 as calculated by Cy48r1, pre-Cy49r1_NOE4C and
336 pre-Cy49r1, with the associated percentage differences being provided in parentheses as e.g. ((pre-Cy49r1-
337 Cy48r1)/Cy48r1) *100. All global budget terms are closed.

Process	Cy48r1	pre-Cy49r1_NOE4C	pre-Cy49r1
Emission	54.0	54.0 (-)	54.0 (-)
DMS + OH → SO_2	21.8	21.8 (-)	21.5 (-1.6)
SO_2 + OH → H_2SO_4	15.1	15.4 (+2.3)	16.5 (+9.3)
SO_2 (aq) → SO_4 (aq)	33.7	33.9 (+1.2)	33.0 (-2.2)
Dry Deposition	21.6	21.3 (-3.0)	22.2 (+3.0)
Wet Deposition	8.2	8.0 (-3.0)	6.9 (-15.8)
Burden	0.70	0.71 (+1.4)	0.75 (+7.1)
Lifetime (days)	3.25	3.29 (+1.2)	3.48 (+7.1)

338
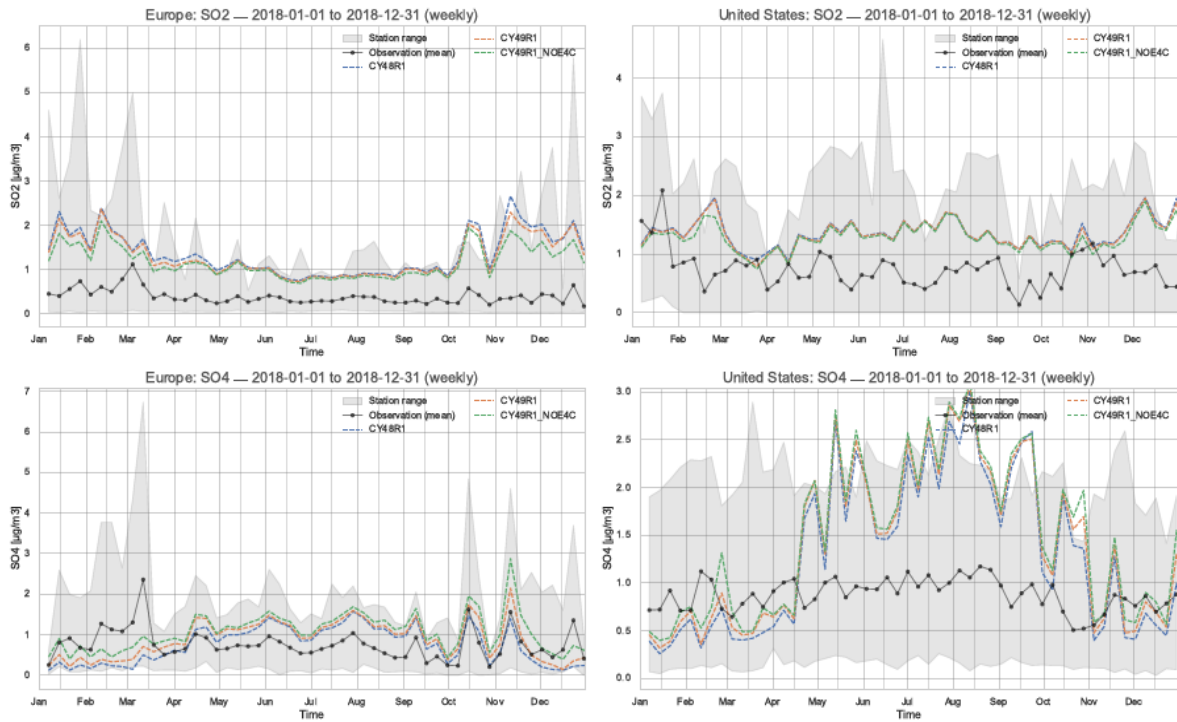
339

340 **Figure 2:** A comparison of weekly mean SO_2 and SO_4^{2-} for Europe (left panels; µg/m³) and the U.S. (right panels)
341 simulated in IFS-COMPO as compared against EMEP and CASTNET observational networks, respectively, for
342 2018. The sampling frequency of the data for SEAsia does not allow a corresponding weekly plot for this region.
343 The grey band shows the station range (min–max) of observed weekly means at each time.

344 In the right-hand panels of Fig. 2 a similar comparison is made against weekly observational composites of surface
345 [SO_2(g)] and [SO_4^{2-}] from the CASTNET measurement network. As for Europe, no seasonal cycle exists in the
346 observations of either surface [SO_2(g)] or [SO_4^{2-}] with typical weekly mean values of around 0.7-1.0 µg/m³. For the
347 wintertime, lower weekly MB occur for both pre-Cy49r1_NOE4C and pre-Cy49r1 as compared with Cy48r1, where
348 the weekly variability is inverse of that seen in the observations. During the summertime much larger positive biases
349 occur, reaching between 200-300% across all IFS-COMPO simulations. Simulated [SO_4^{2-}] exhibits a strong seasonal
350 cycle despite no such increase in the simulated [SO_2(g)]. Although some small differences in the SO_2(g) weekly values
351 occur between simulations, there is no improvement in pre-Cy49r1 with respect to the weekly MB. The positive
352 summertime MB for SO_2 implies that there is either an overestimate in the regional source terms or an underestimate
353 in the depositional loss term (c.f. [SO_4^{2-}] below)

354 Figure 3 shows the yearly means of surface [SO_4^{2-}] for Cy48r1 and pre-Cy49r1 for Europe (top panels), the U.S.
355 (middle panels) and Southeast Asia (bottom panels). The changes in surface [SO_4^{2-}] here are somewhat unaffected by
356 the changes in PM2.5 due to EQSAM4Clim that are shown in Rémy et al. (2024) for 2019, due to the dominant
357 aqueous-phase production term (albeit with small increases due to the additional contribution from organic acids). One
358 main difference for SO_x than either NH_x or NO_x, is that the gas-particle partitioning is dependent on cloud pH, dissolved
359 O_3 and hydrogen peroxide (H_2O_2), where SO_4^{2-} production is irreversible.

360 For Europe, a sharp north-south gradient exists imposed by the variability in H_2SO_4 production between seasons, cloud
361 cover for the wet production term and the distribution of the primary point sources for SO_2 emissions, although
362 mitigation measures remove the increase in the emitted flux during the cold winter months associated with domestic
363 heating (Versteeg et al., 2007). Simulated concentrations in Cy48r1 are lower in Scandinavia as compared with e.g.
364 France, which results in a low bias of around 1 µg/m^3 in e.g. Finland and around the Baltic, here related to missing
365 shipping emissions of SO_2, which quickly converts to SO_4^2 in the plume (Celik, et al., 2020). For the other sites in
366 Europe agreement is better with the low bias decreasing to approx. 0.5 µg/m^3. One outlier exists for the most easterly
367 station, which exhibits a significant high bias of 1.5 µg/m^3. Comparing pre-Cy49r1 shows increases in the simulated
368 surface [SO_4^{2-}] of between 0.2-0.4 µg/m^3, which leads to an improved bias. Only small improvements are made to the
369 correlation coefficient due to identical emission estimates being used and EQSAM4Clim affecting SO_x the least, i.e.,
370 only indirectly through changes in pH.

371 For the U.S., the CASTNET observations show an east-west continental gradient in surface [SO_4^{2-}] exists as determined
372 by the distribution in the primary SO_2 emissions and transport (c.f. Figure 1). A significant transport component exists
373 for SO_4^{2-}, resulting in surface [SO_4^{2-}] in the Marine Boundary Layer between 1.0-2.5 µg/m^3, where transport dominates
374 local surface [SO_4^{2-}] produced from DMS oxidation (Simpson et al., 2014). For pre-Cy49r1 there is a reduction in
375 surface [SO_4^{2-}] at continental scale, with a decrease in the yearly MB from 0.67 to 0.20 µg/m^3, with a corresponding
376 increase in the correlation coefficient to 0.43, albeit remaining only rather weakly correlated. For the West of the U.S.
377 a positive MB is introduced for the rural background in pre-Cy49r1 of 0.5-0.7 µg/m^3, with a contribution being
378 transported from the east. Hence, reductions in the yearly MB primarily stem from improved agreement at Eastern U.S.
379 monitoring sites. That a positive MB of approx. 1-1.5 µg/m^3 exists in the yearly mean values around
380 Kentucky/Tennessee suggests that the local SO_2 emission estimates are too high (see Discussion in Sect. 5).

381 For Southeast Asia, the scarcity of sampling sites in the EANET network results in a less robust evaluation. Many
382 sampling sites are located at coasts rather than inland, thus the influence of changes at coastal regions has an influence
383 on the regional statistics. Higher primary SO_2 emissions occur on the land. Therefore, any positive MB near source
384 regions is not included in the statistics; the results shown here for surface SO_4^{2-} should be considered lower limits.
385 The long-range transport of SO_4^{2-} in Asia has been shown to somewhat neutralise national SO_2 mitigation measures
386 taken in e.g. Taiwan and South Korea. This originates from changing trends in SO_2 emission from mainland China as
387 captured by EANET measurement sites (Chang et al, 2022). For Cy48r1 the yearly mean statistics show an
388 exceptionally low MB and a good correlation coefficient of 0.75. For pre-Cy49r1 there is a significant degradation,
389 where the MB increases to 0.48 µg/m^3 showing a trend in the performance for SO_x that is like the U.S. . Notably, the
390 more remote sampling stations (e.g. oceanic) exhibit regional negative biases (approx. -0.7 µg/m^3) whereas those
391 situated near Mongolia and South Korea agree well with low MB values. For Thailand and Vietnam there are typically
392 large MB values, suggesting regional SO_2 emission estimates are too high. Unfortunately, there are no in-situ
393 measurements available for better quantification. The correlation coefficient degrades in pre-Cy49r1 compared to
394 Cy48r1 towards 0.66. Overall, the improvements are mixed for the SO_2 - SO_4^{2-} couple and much less pronounced
395 compared to the other SIA.

396

397
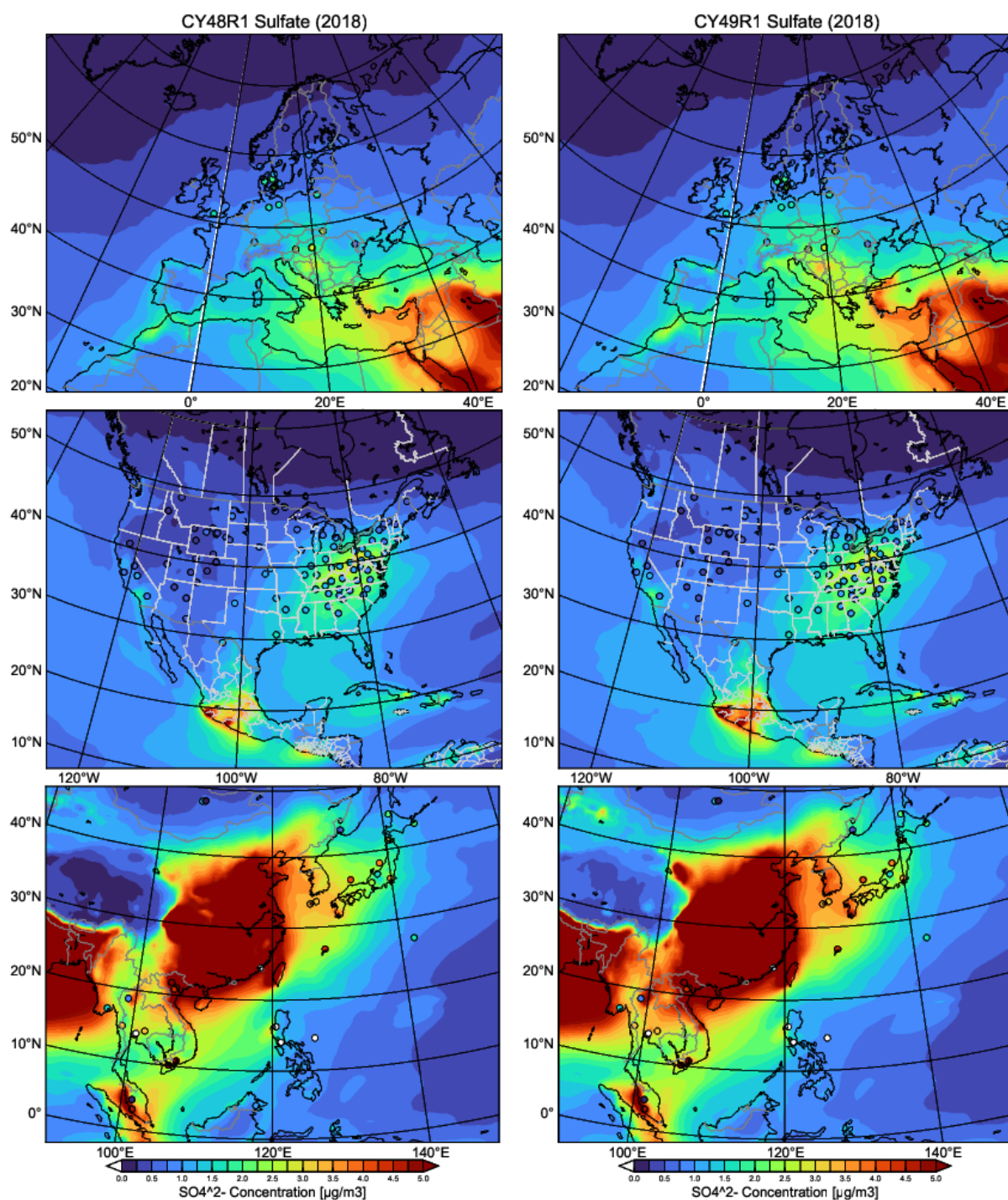
Figure 3: Comparisons of yearly mean [SO$_4^{2-}$] simulated at the surface in Cy48r1 and pre-Cy49r1 when compared against measurements for the three selected regions during 2018 (µg/m^3). The corresponding regional statistics are provided in Table 3. Site locations and observed values, taken from the EMEP, CASTNET and EANET networks respectively, are shown in circles.

402

Table 3 : The yearly MB, RMSE and Pearsons R values for the comparisons of the daily (EMEP, Europe), weekly (CASTNET, US) and yearly (EANET, Southeast Asia) mean regional distributions and concentrations of surface SO$_4^{2-}$ as compared against composites assembled from the observations for 2018 shown in Fig. 3 for Europe, the U.S. and Southeast Asia. Percentage differences are calculated as ((pre-Cy49r1-Cy48r1)/Cy48r1) *100 and given in parentheses.

	Europe (EMEP)		US (CASTNET)		SE Asia (EANET)	
$SO_4^=$	Cy48r1	pre-Cy49r1	Cy48r1	pre-Cy49R1	Cy48R1	pre-Cy49R1
MB ($\mu g/m^3$)	-0.49	-0.32 (-35)	0.67	0.20 (-70)	-0.02	0.48 (+96)
RMSE	1.35	1.31 (-3)	0.93	0.46 (-50)	1.64	2.28 (+39)
Pearsons R	0.45	0.47 (+4)	0.33	0.43 (+23)	0.75	0.66 (-12)

408

409   **4.2 NH$_3$ and NH$_4^+$**

410   The regional distribution of surface NH$_3$ for 2018 in the three chosen global regions and the resulting changes for pre-
411   Cy49R1_NOE4C and pre-Cy49r1 are shown in Figure 4. Although there is a declining trend in European regional
412   NH$_3$ emissions (Tichý et al, 2023), a strong seasonal cycle exists in Cy48r1. Maximal mixing ratios are situated around
413   Benelux and northern Italy, with local differences of 8-20 ppb between July and December across regions. The
414   CAMS_GLOB_ANT v5.3 (Soulie et al, 2024) emission inventory has recently been validated for NH$_3$ against top-
415   down estimates providing confidence in the quality of the estimates for Europe (Ding et al., 2024). For the U.S., a
416   similar seasonal signature exists especially for the northwest and southeast associated with agricultural emissions
417   (Wang et al, 2020), with background mixing ratios of between 0.5-2.0 ppb remaining constant. For China, whose NH$_3$
418   emissions have increased over the last decades (Liu et al., 2019; Chen et al. 2023), surface mixing ratios of between
419   5-20 ppb occur for July for large areas, again associated with agricultural practices. Likewise, high mixing ratios are
420   found around Bangladesh (> 20 ppb). For December, mixing ratios are typically an order of magnitude lower, except
421   for the Southwest, which again exhibits high mixing ratios (> 20 ppb). Measurements of NH$_x$ over the ocean are rare,
422   thus the substantial increase which is simulated in pre-Cy49r1 cannot be evaluated. Nevertheless, estimates range
423   from 0.1-4.2 ppb depending on season and location (Sharma et al., 2012) indicating that Cy48r1 has a significant
424   negative bias which is somewhat improved in pre-Cy49r1.

425   Table 4 provides the global budget terms for all three simulations, showing the significant increase in deposition terms
426   and tropospheric burden for NH$_3$(g). For pre-Cy49r1, the improved gas/particle partitioning from EQSAM4Clim
427   reduces the particle phase concentrations of the semi-volatile aerosol species which leads to an increase in the
428   respective gas phase concentrations, also affecting aerosol pH. This determines the solubility of NH$_3$(g), also
429   contributing to its reduced conversion into NH$_4^+$ (see Table 4, approx. 44% reduction), which is an effect amplified
430   by the inclusion of mineral cations (i.e. Ca^{2+}, Na$^+$, K$^+$, Mg^{2+}). The tropospheric lifetime of NH$_3$(g) more than doubles
431   in pre-Cy49r1 allowing more transport from strong source regions, in line with changes in the tropospheric burden.
432   Both the associated loss due to dry and wet deposition increases (37% and 51%, respectively), due to lower NH$_4^+$
433   particle production (see Sect. 4.2).

434   Figure 5 shows comparisons between weekly observational composites from EMEP of [NH$_3$(g)] against those
435   extracted from the various IFS-COMPO simulations for 2018. The observational composite shows that there is a
436   skewed seasonal cycle exhibiting a maximum in April/May from agricultural activity, with wintertime values being
437   around 0.4-0.5 $\mu g/m^3$ increasing to 0.8-1.5 $\mu g/m^3$ during spring and summertime. This seasonal variability is captured
438   across all simulations with a high correlation with a Pearsons's R value between 0.71-0.73. For wintertime there is
439   limited variability and an associated low weekly bias of around 0.1$\mu g/m^3$. For summertime, there is a weekly bias of
440   between 0.5-1.0 $\mu g/m^3$ in Cy48r1 (yearly MB of approximately 0.5 $\mu g/m^3$), with the MB almost doubling for pre-
441   Cy49r1 (with a yearly MB of approximately 0.7 $\mu g/m^3$.

442   **Table 4**. The tropospheric NH$_3$ budget in Tg N/year for 2018 as calculated by Cy48r1, pre-Cy49r1_NOE4C
443   and pre-Cy49r1, with the associated percentage differences being provided in parentheses as e.g. ((pre-Cy49r1-
444   Cy48r1)/Cy48r1)*100. All global budget terms are closed.

Process	Cy48r1	pre-Cy49r1_NOE4C	pre-Cy49r1
Emission	51.1	51.1 (-)	51.1 (-)

NH$_3$ + OH	0.82	0.99 (+20)	1.98 (+240)
NH$_3$ → NH$_4^+$	30.6	30.3 (-1)	17.3 (-44)
Dry Deposition	16.3	16.6 (+2)	22.4 (+37)
Wet Deposition	7.0	6.2 (-13)	10.6 (+51)
Burden	0.13	0.16 (+19)	0.29 (+118)
Lifetime (days)	0.9	1.1 (+22)	2.0 (+133)

445

446   The bottom left panel of Fig. 5 shows the corresponding comparisons of [NH$_4^+$] in Europe using the weekly
447   observational means from the EMEP network. There is a reversed seasonality for [NH$_4^+$] with higher [NH$_4^+$] during
448   wintertime due to the colder temperatures decreasing the volatility of the particles (e.g. Tang et al., 2021). Moreover,
449   for Cy48r1 there is clearly a large positive bias of [NH$_4^+$] with only minor changes introduced due the wet scavenging
450   in pre-Cy49r1_NOE4C. Wintertime biases are reduced in pre-Cy49r1 especially for weeks which exhibit peaks in the
451   observational means which IFS-COMPO can capture.

452   Similar comparisons are shown for the U.S. in the bottom right panel of Fig. 5 using weekly composites assembled
453   from the CASTNET data. In contrast to the seasonal cycle for [NH$_3$(g)], which peaks during April/May, there is no
454   corresponding seasonal cycle in the weekly [NH$_4^+$] values peaks, being consistent between 0.4-0.5 μg/m^3 during
455   summertime. This indicates that a saturation occurs with respect to NH$_4^+$ particle formation which is linked to
456   availability of HNO$_3$(g) (c.f. See sect 4.3. below). Again, significant biases exist in Cy48r1 and pre-Cy49r1_NOE4C,
457   reaching around 1.0 μg/m^3 during summertime (which is 200% of the summertime observational values). Applying
458   EQSAM4Clim essentially removes this positive MB in pre-Cy49r1, resulting in good agreement for the entire year.

459

460

461
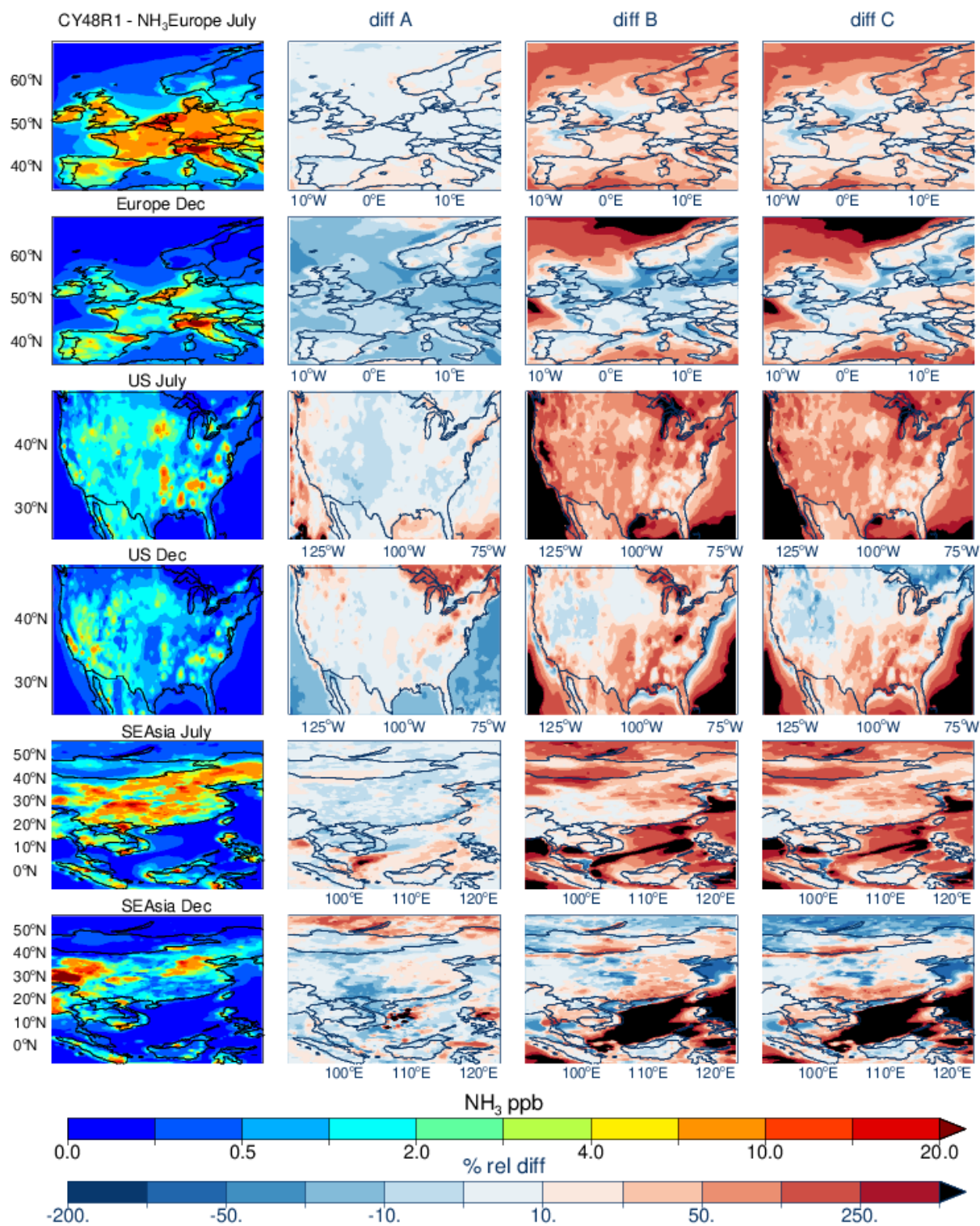
Figure 4: As for Fig. 1 except for NH₃. Panel definitions: Diff A=(pre-Cy49r1_NOEQ4C - Cy48r1)/Cy48r1;
Diff B=(pre-Cy49r1-Cy48r1)/Cy48r1 and Diff C=(pre-Cy49r1-pre-Cy49r1_NOEQ4C)/Cy48r1.
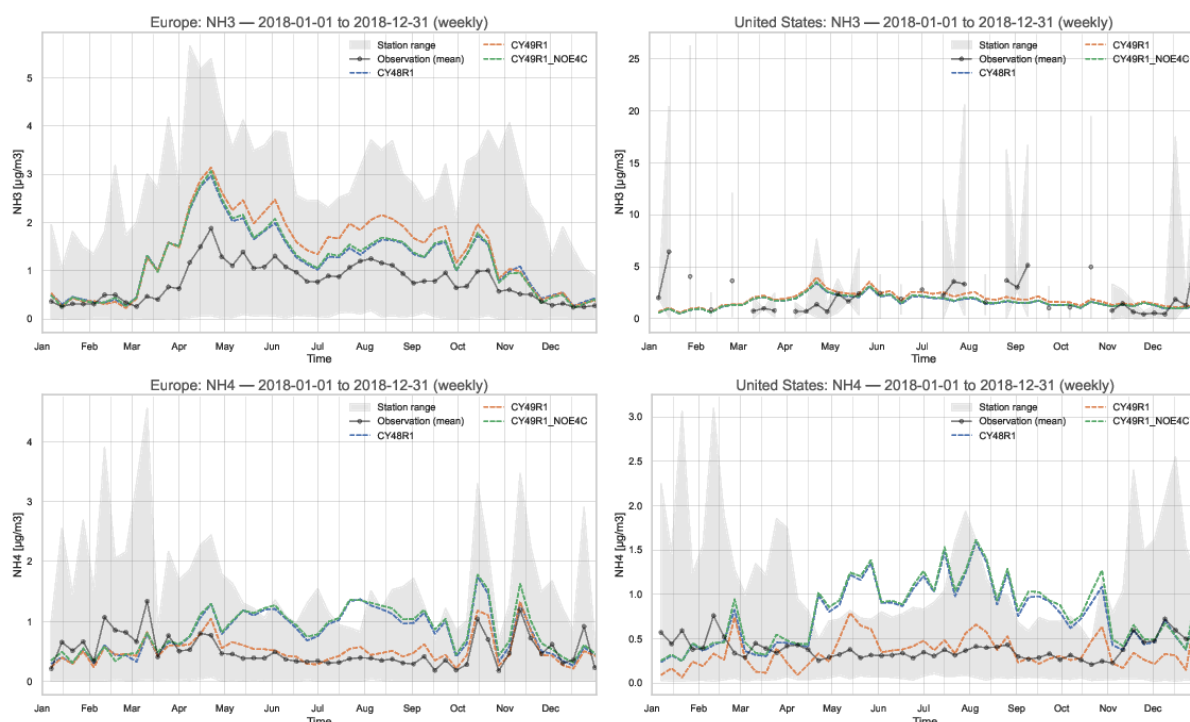
Figure 5: A comparison of weekly mean $[NH_3(g)]$ and $[NH_4^+]$ at the surface for Europe (left panels; $\mu g/m^3$) and the U.S. (right panels) as simulated in IFS-COMPO as compared against the composites of measurements taken from EMEP and CASTNET for 2018. For the U.S., the data for $NH_3(g)$ is taken from the AMoN measurement network in the top right panel. The data frequency provided for the Southeast Asia region does not allow a corresponding plot, although yearly statistics are provided in Table 5. The grey band shows the station range (min–max) of observed weekly means at each time.

Table 5: As for Table 3 except for NH_4^{+-}.

NH_4^+	Europe (EMEP)		US (CASTNET)		SE Asia (EANET)	
	Cy48r1	pre-Cy49r1	Cy48r1	pre-Cy49r1	Cy48r1	pre-Cy49r1
MB ($\mu g/m^3$)	0.26	-0.05 (-81)	0.95	0.23 (-48)	0.96	0.55 (-43)
RMSE	0.94	0.72 (-23)	1.71	0.46 (-73)	1.73	1.30 (-25)
Pearsons R	0.46	0.62 (+29)	0.59	0.43 (-27)	0.59	0.44 (-25)

Figure 6 shows the distribution of the corresponding yearly mean $[NH_4^+]$ for the three chosen regions for both Cy48r1 and pre-Cy49r1 during 2018, with the associated regional yearly mean statistics being given in Table 5. The location of the measurement sites is shown in each panel, with the respective yearly mean values within each circle. Significant decrease in the conversion rate of NH_3 in pre-Cy49r1 results in lower $[NH_4^+]$. This is a result of the improved gas/aerosol partitioning and the subsequent increase in aerosol pH when applying EQSAM4Clim (see Table 4; Rémy et al., 2024). More direct depositional loss to the surface for $NH_3(g)$ occurs in pre-Cy49r1 due to increased residence time. There is a wide variability in the simulated aerosol pH between regions, with Europe exhibiting aerosol pH values of around 3-4, whereas the southern U.S. and northern China exhibit aerosol pH values in the range 2-3 (Pan et al, 2024; Rémy et al, 2024) which indirectly affects the temporal variability in NH_4^+ production. Once formed, regional transport contributes to the continental distribution of NH_4^+ away from strong source regions (e.g. Simpson et al., 2010; Renner and Wolke, 2010; Du et al, 2020).

For Europe (top panels), most observational yearly mean values are between 0.2-1.2 $\mu g/m^3$ which are exceeded by > 50% in Cy48r1. In pre-Cy49r1 the reductions in the yearly mean $[NH_4^+]$ are of the order of 0.5-1.0 $\mu g/m^3$ and result in low yearly mean $[NH_4^+]$ values for e.g. Spain/UK, whilst reducing maximal concentrations by approx. 50% in

northern Italy. This subsequently contributes to a reduction in the cumulative PM2.5 biases for this region as shown in Rémy et al. (2024) for 2019. The associated MB values in Table 5 show a significant reduction in the bias (> 80%) along with an increase in the correlation coefficient, although the simulated NH_4^+ distribution is still only moderately correlated (r=0.62). Unfortunately, the lack of available measurements means no quantification of the performance of IFS-COMPO around the mediterranean can be shown. It should be noted that with a more realistic distribution and seasonal variability in $NH_3(g)$ emissions (e.g. Shepard et al, 2011; Dammers et al, 2019), the $[NH_4^+]$ distributions shown here will not be affected as other SIA species determine the $NH_3 - NH_4^+$ gas/aerosol partitioning.

For the U.S. (middle panels) similar decreases in yearly mean $[NH_4^+]$ values occur in pre-Cy49r1 as compared to Cy48r1, with very low concentrations of between 0.1-0.4 $\mu g/m^3$ for the west of the U.S., which shows less bias when compared against the observational mean values. This causes a reduction in the yearly mean regional bias of around 0.7 $\mu g/m^3$ as shown in Table 5. A gradient exists in the aerosol pH from EQSAM4Clim ranging from yearly mean values of pH=3.0 towards the northwest of the U.S. and becoming more acidic towards the southwest U.S. with yearly mean values of pH=2.0 (Rémy et al., 2024). This reduces the transfer of $NH_3(g)$, thus moderating NH_4^+ production (c.f. Table 5). For the northeast of the U.S. with high NO_x emissions, there are reductions of between 0.5-1.0 $\mu g/m^3$. For the South-western U.S., with high $[NH_3(g)]$ from agriculture (c.f. Fig. 5) there are reductions of between 0.3-1.0 $\mu g/m^3$. There is a degradation in the correlation coefficient exhibiting a moderate yearly mean correlation with significant overestimates for the South-western U.S. as shown for the comparisons of $[NH_3(g)]$ at selected sites in Figure 5.

For Southeast Asia (bottom panels), the simulated yearly mean $[NH_4^+]$ over land are typically much higher than those simulated for either Europe or the U.S., with maximal values of between 7.0-9.0 $\mu g/m^3$ for eastern China, in-spite of the similar surface mixing ratios in $NH_3(g)$ between Europe and China as shown in Fig. 5. This difference is predominantly driven by the relatively high $HNO_3(g)$ in China due to the more polluted chemical regime (the availability of $O_3(g)$, $NO_2(g)$ and $OH(g)$ determining gas-phase $HNO_3(g)$ production). Applying EQSAM4Clim in pre-Cy49r1 results in significant decreases of between 1-2 $\mu g/m^3$ $[NH_4^+]$ as associated with the highest yearly mean $[NH_4^+] > 6.0$ $\mu g/m^3$. This reduces the associated yearly mean regional bias by 0.4 $\mu g/m^3$, with a corresponding reduction in the correlation, due to less transport. Again, the lack of sampling sites in the region with high primary $NH_3(g)$ emissions skews the associated yearly mean biases. For the more remote locations (e.g. Mongolia/South China Sea) low values of < 0.5 $\mu g/m^3$ are captured well in both Cy48r1 and pre-Cy49r1.
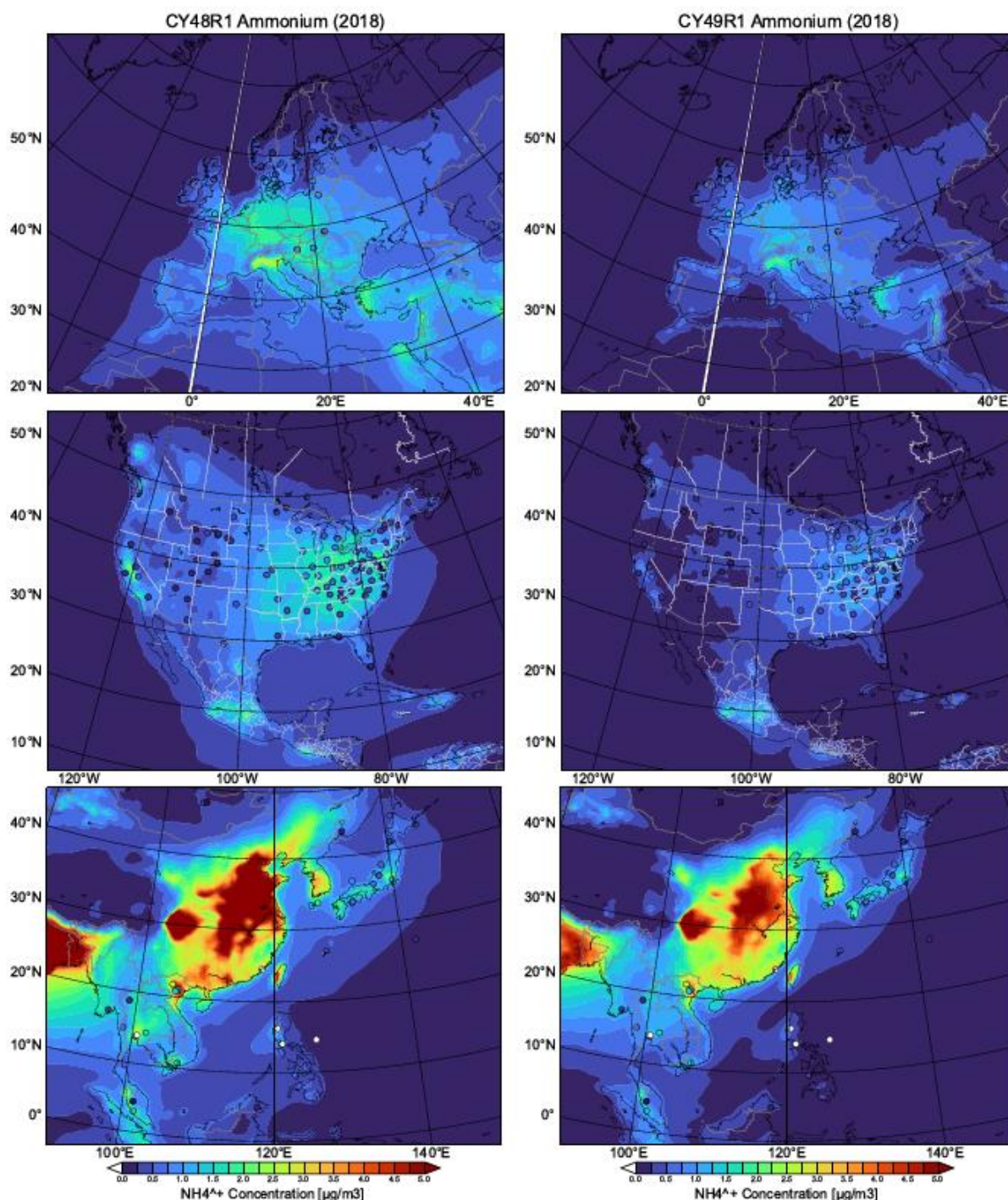
Figure 6: Comparisons of yearly mean [NH$_4^+$] simulated at the surface in Cy48r1 and pre-Cy49r1 when compared against measurements for the three selected regions during 2018 (µg/m^3). The corresponding regional statistics are provided in Table 5. Site locations and observed values, taken from the EMEP, CASTNET and EANET networks respectively, are shown in circles.

4.3 HNO$_3$ and NO$_3^-$

Figure 7 shows the monthly mean distributions and mixing ratios of HNO$_3$(g) for July and December 2018 for the three chosen global regions for Cy48r1, along with the relative differences when compared with pre-Cy49r1_NOE4C and pre-Cy49r1. The corresponding global chemical budget terms for HNO$_3$(g) during 2018 are provided in Table 6. No direct emission of HNO$_3$ occurs in IFS-COMPO, which is often prescribed in global

1739

chemistry transport models to represent e.g. chemistry in the plumes of ships (e.g. Vinken et al., 2011), with the main source being the oxidation of NO_2 by OH in the gas-phase as shown in Table 6. This production term increases in pre-Cy49r1 by approx. 14% because of the enhancements in OH via changes in O_3 (not shown). For heterogeneous conversion, the cumulative HNO_3 production term is approximately 50% that of the gas-phase production term, remaining relatively constant between simulations. There is a shift between fine mode NO_3^- (NH_4NO_3) and coarse mode NO_3^- ($CaNO_3/NaNO_3$), strengthening the link between NH_4^+ and NO_3^- in pre-Cy49r1. Both dry and wet loss terms increase significantly due to the increase in the availability of $HNO_3(g)$, which reduces the fraction converted to NO_3^-. The temporal variability of $HNO_3(g)$ is influenced by the magnitude and extent of regional NO_x emissions, photochemical activity (via OH formation), gas/aerosol partitioning (where particles with high $SO_4^=$ content having an associated low NO_3^- content) and scavenging in clouds and aerosols.

For Europe very low surface mixing ratios occur over land for both months shown in Cy49r1 (< 0.1 ppb), which is surprising considering that the Benelux has been shown to have high NO_x levels (van der A, 2024) therefore likely to have correspondingly high $HNO_3(g)$ mixing ratios. Higher mixing ratios of between 0.25-0.5 ppb occur around the Coasts and the Mediterranean originating from direct shipping emissions of NO_2. This can lead to elevated NO_3^- concentration due to uptake of $HNO_3(g)$ on sea salt, which might be too high as the current formulation of EQSAM4Clim only assumes thermodynamic equilibrium which is not dynamically limited. Here, an aerosol dynamical model refers to a microphysical framework that prognoses particle number/size distributions (via condensational growth, coagulation, nucleation and inter-mode transfer), thus enabling kinetically limited gas-to-particle uptake and condensation processes beyond the instantaneous thermodynamic equilibrium assumed by EQSAM4Clim (Metzger et al., 2018). A coupling with a dynamical aerosol model is foreseen for future versions of IFS-COMPO. In contrast, the application of EQSAM4Clim in pre-Cy49r1 results in large increases in surface $HNO_3(g)$ at continental scale during July. For December, the relative differences in pre-Cy49R1 compared to Cy48r1 show increases in HNO3(g) at latitudes below 60°N, together with decreases of between 25-75% at latitudes higher than 60°N, i.e. at lower temperatures, and under a relatively low NOx environment.

For the U.S., the highest $HNO_3(g)$ mixing ratios in Cy48r1 occur for the eastern states and California (1-2 ppb), with much lower values in the more remote central U.S. (0.1-0.2 ppb), with a strong seasonal cycle in maximal values peaking in July. Comparing relative differences between simulations shows a significant increase of surface $HNO_3(g)$ in pre-Cy49r1 (between 0.1-6 ppb) at continental scale for both months, with the largest increases occurring in the northern States. In contrast to Europe no significant decreases in $[HNO_3(g)]$ occur for any location or season.

Finally, in comparison to the other regions the surface $[HNO_3(g)]$ are highest for Southeast Asia. Maximal mixing ratios of 4-5 ppb occur towards the eastern coast (July) and central regions (c.f. December). Comparing the relative differences between simulations shows significant increases of between 50-5000%, apart from the more remote regions to the north where NOx emissions are lower. As for Europe, a strong seasonality can be seen with decreases above 30°N occurring regardless of the NO_x regime. As shown for NH_3 (c.f. Fig. 4), there are significant increases in HNO_3 over the ocean for both months shown, associated with lower $[NO_3^-]$ (as shown by the cumulative reduction in global conversion by 50%).

Figure 8 shows the resulting changes in surface $[HNO_3(g)]$ across simulations for Europe when compared against weekly means from the EMEP measurement sites (top left panel). The location of these sites is shown in Figure A1 in the Appendix, where the location of the sampling sites results in a significant bias in the evaluation towards northern Europe. No obvious seasonal cycle is evident in the observational weekly means, with concentrations in the range of 0.3-0.7 $\mu g/m^3$, although many sites are located away from strong NO_x sources. Both Cy48r1 and pre-Cy49r1_NOE4C exhibit negative weekly biases resulting in under-estimations of around 100% in concentrations during the summertime, although the weekly variability is captured to a degree. There is a reduction in the bias of around 0.2-0.4 $\mu g/m^3$ in pre-Cy49r1_NOE4C due to changes in the gas-phase production term. (c.f. Table 8). For pre-Cy49r1 there is a significant excess of $[HNO_3(g)]$ due to enhanced production and less transfer into the particulate phase, despite an increase in the cumulative deposition terms. Such changes are associated with relatively low $[HNO_3(g)]$ IFS-COMPO values of around < 0.1 ppb.
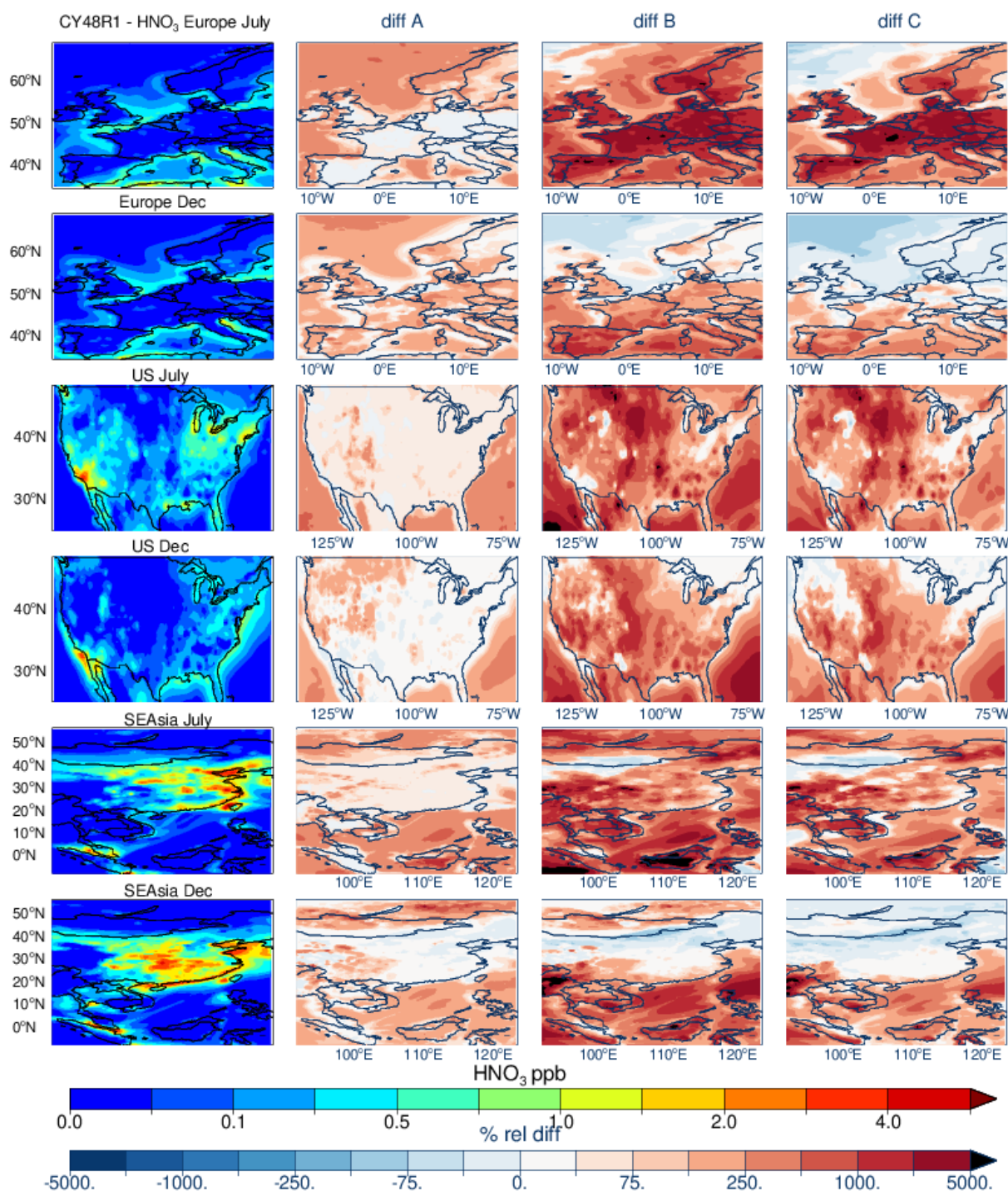
Figure 7: As for Fig. 1 except for HNO₃. Panel definitions: Diff A = (pre-Cy49r1_NOEQ4C - Cy48r1)/Cy48r1; Diff B = (pre-Cy49r1-Cy48r1)/Cy48r1 and Diff C = (pre-Cy49r1-pre-Cy49r1_NOEQ4C)/Cy48r1.

Figure 8 also shows comparisons of weekly [HNO₃(g)] from the CASTNET measurement network in the U.S. (top right panel). As for Europe, both the concentrations and seasonal variability in the observations is low, with typical weekly concentrations being approximately 0.5 μg/m³. The homogeneous distribution of measurement sites in the U.S. means the evaluation presented does not have any significant regional bias. That the observed weekly mean concentrations are rather constant is surprising considering that variability in the gas-phase chemical production term involves OH. However, changes in RH, temperature and NH₃(g) across seasons also contribute to the seasonal lifetime. In contrast to Europe, both Cy48r1 and pre-Cy49r1_NOE4C show good agreement against the measurements with weekly biases of the order of 0.2-0.25 μg/m³. However, for pre-Cy49r1 a large positive bias is introduced directly from the use of EQSAM4Clim due to a limitation in the ability for HNO₃ to condense on

587   particle surfaces. This means that condensed HNO_3 does not contribute to NH_4NO_3 formation (which requires a
588   coupling of EQSAM4Clim with an aerosol dynamical model) as proposed for future cycles of IFS-COMPO. It
589   also shows that although the cumulative global dry and wet deposition terms in pre-Cy49r1 have increased
590   markedly compared to Cy48r1 (c.f. Table 6), fluxes are not large enough to compensate for the reduced aerosol
591   formation.

592   **Table 6:** The tropospheric HNO_3 budget in Tg N/year for 2018 as calculated by Cy48r1, pre-Cy49r1_NOE4C and
593   pre-Cy49r1, with the associated percentage differences being provided in parentheses as e.g. ((pre-Cy49r1-
594   Cy48r1)/Cy48r1)*100. All global budget terms are closed.

Process	Cy48r1	pre-Cy49r1_NOEQ4Clim	pre-Cy49r1
$NO_2 + OH \rightarrow HNO_3$	11.0	11.6 (+5)	12.6 (+14)
$N_2O_5 + Liq \rightarrow HNO_3$	2.2	2.5 (+12)	2.6 (+17)
$N_2O_5 + Aer \rightarrow HNO_3$	3.2	2.3 (-28)	2.3 (-27)
$NO_3 + Aer \rightarrow HNO_3$	0.8	0.4 (-47)	0.5 (-42)
$HNO_3 \rightarrow$ Fine NO_3^-	1.4	1.2 (-18)	2.0 (+41)
$HNO_3 \rightarrow$ Coarse NO_3^-	9.3	5.9 (-36)	3.6 (-61)
Dry Deposition	2.0	2.4 (+17)	5.1 (+150)
Wet Deposition	6.8	5.9 (-13)	9.3 (+38)
Trop. Burden	0.31	0.30 (-3)	0.32 (+3)

595

596   Figure 8 also shows the corresponding changes in surface $[NO_3^-]$ for Europe (bottom left panel). The observational
597   composites show that $[NO_3^-]$ has concentrations almost twice those of the corresponding $[HNO_3(g)]$ during
598   wintertime. For summertime there is almost an equal split in the phase partitioning between precursor and SIA.
599   Unlike for $HNO_3(g)$, a shallow concave seasonal cycle exists in the weekly observational composites, related to
600   seasonal differences in temperatures and lifetime (Tang et al., 2021). Both Cy48r1 and pre-Cy49r1_NOE4C fail
601   to capture the correct seasonality and exhibit higher concentrations during summertime, resulting in substantial
602   positive biases of 1-2 $\mu g/m^3$. Considering the associated biases in $[HNO_3(g)]$ shows that the HNO_3-NO_3^-
603   partitioning is not captured well. For pre-Cy49r1 the description of the seasonal cycle is significantly improved
604   due to the inclusion of EQSAM4Clim, resulting in much lower biases of < 0.5 $\mu g/m^3$ throughout the year, also
605   pointing to the importance of a better representation of gas/particle partitioning. The corresponding changes in
606    $[NO_3^-]$ in the simulations are evaluated against weekly composites from the CASTNET measurement network are
607   shown in the bottom right panel of Fig. 8. A similar seasonal cycle exists as for Europe with similar concentrations.
608   For Cy48r1 and pre-Cy49r1_NOE4C an inverse seasonal variability occurs in $[NO_3^-]$ as compared with the
609   observational weekly means, resulting in significant positive biases of around 1.0-1.5 $\mu g/m^3$. For pre-Cy49r1
610   biases decrease by an order of magnitude and the seasonal variability is improved markedly, again showing
611   improved particle distribution when using EQSAM4Clim.

612
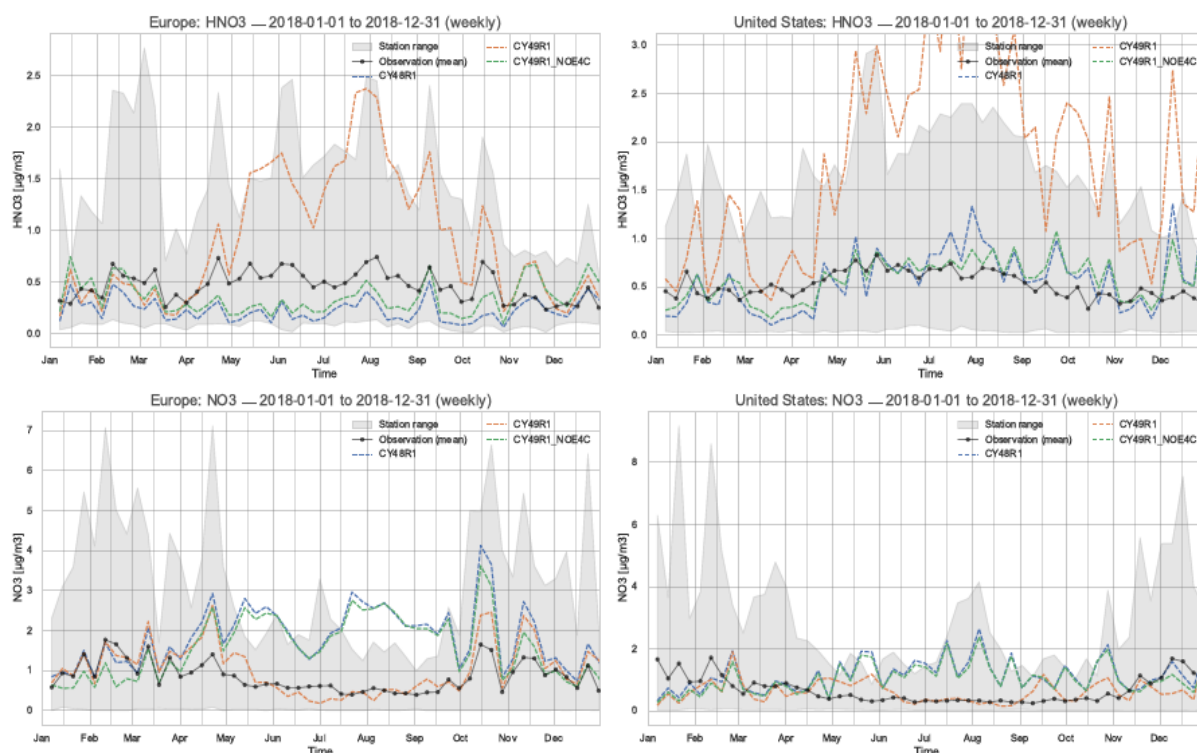
Figure 8: A comparison of weekly mean [HNO$_3$(g)] and [NO$_3^-$] for Europe (left panels; μg/m^3) and the U.S. (right panels) at the surface as simulated in IFS-COMPO as compared against measurement composites from EBAS (left) and CASTNET (right) stations for 2018. The grey band shows the station range (min–max) of observed weekly means at each time.

In Figure 9 we show the corresponding regional distributions of the yearly mean [NO$_3^-$] for Cy48r1 and pre-Cy49r1 during 2018 for the three chosen global regions, where the associated changes in the regional yearly mean statistics are provided in Table 7. Some commonality exists between the changes shown for yearly mean [NH$_4^+$] and yearly mean [NO$_3^-$], due to the speciation of the SIA involved. The cumulative sums of the smaller NO$_3^-$ particle (fine mode NO$_3^-$ in Table 6 with the form NH$_4$(NO$_3$)) and the larger NO$_3^-$ particle (coarse mode NO$_3^-$ in Table 6 with the form of CaNO$_3$ and NaNO$_3$) are both included in the plots. Therefore, the changes evaluated here are a combination of changes to both the fine and coarse mode NO$_3^-$, rather than the changes associated with individual particle sizes. In contrast to the reduced N analysis provided above, which is impacted more directly due to changes in the fine mode NO$_3^-$, with [NO$_3^-$] also indirectly affected by the coarse mode assumptions through the effect of cations on the neutralisation level that subsequently controls the gas/aerosol equilibrium partitioning. The change in the partitioning for HNO$_3$ shown above results in an associated reduction in the fraction of NO$_x$ held in particulate form due to e.g. a higher dry deposition component.

For Europe, the simulated yearly mean [NO$_3^-$] in Cy48r1 generally ranges between 0.2-2.0 μg/m^3 over Scandinavia/Spain and the surrounding seas and between 2.0-6.3 μg/m^3 over northwestern/central Europe and the Mediterranean, becoming lower towards the northeast and southwest. The highest European NO$_x$ emissions occur around the south-east of the UK, Benelux, the Ruhr, and Po valleys (e.g. Liu et al., 2021; van der A., 2024). This, and the rather homogeneous distribution within central Europe shows that a significant degree of transport occurs once NO$_3^-$ particles are formed. No such continental gradient in the yearly mean [NO$_3^-$] exists in the observational mean values indicating an overestimate in IFS-COMPO. Nevertheless, in pre-Cy49r1 decreases in [NO$_3^-$] of between 2-4 μg/m^3 occur for the Baltic states/France/Germany and over the Mediterranean Sea (from relatively high shipping NO$_x$ emissions) compared to Cy48r1. This results in much better agreement with the yearly mean observed values for the individual measurement stations. The yearly regional MB is reduced by $\cong$ 90%, decreasing to 0.1 μg/m^3 in pre-Cy49r1 with an associated increase in the correlation coefficient due to lower transport of [NO$_3^-$] out of the main source region. A large impact occurs due to the acidification of sea salt aerosols under high NO$_x$ emission from dense shipping lanes, which can be seen by similar [NO$_3^-$] reductions over the sea, though difficult to evaluate due to the lack of sufficient in-situ measurements.

644 For the U.S., there is a similar impact on [NO$_3^-$] as shown for Europe, where the high yearly MB in [NO$_3^-$] decreases
645 significantly (94%) from Cy48r1 to pre-Cy49r1 (bottom right panel of Fig. 8). For Cy48r1, [NO$_3^-$] typically ranges
646 between 2-4 µg/m^3 with medium-range transport resulting in appreciable concentrations over the surrounding
647 oceans. There is surprisingly little variability in the observed yearly mean [NO$_3^-$] despite the large difference in
648 the resident [HNO$_3$(g)] across different states of the U.S. related to the distribution of the NO$_x$ emissions (Figure
649 7; Goldberg et al., 2021). Only in the southwest, around California, the yearly mean [NO$_3^-$] > 2.0 µg/m^3, shows
650 typical yearly mean [NO$_3^-$] being ≤ 1.0 µg/m^3 in pre-Cy49r1 for most of the U.S. This implies that the cations
651 used as input for EQSAM4Clim imposes a limit concerning the phase-transfer of HNO$_3$(g) into more acidic
652 aerosols via neutralisation of the anions by cations in the particle phase.

653
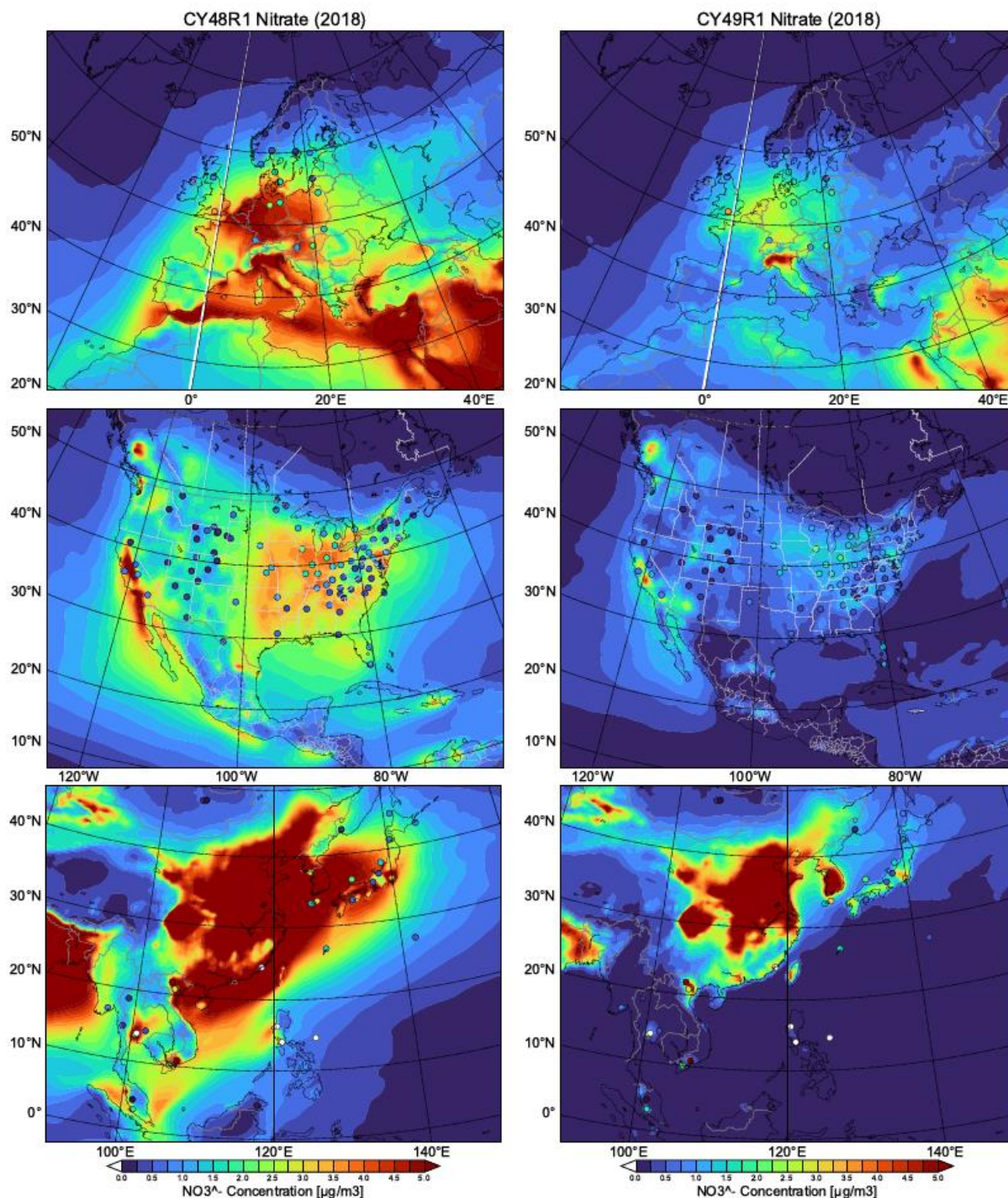
654 **Figure 9:** Comparisons surface comparisons of [NO$_3^-$] simulated in Cy48r1 and pre-Cy49r1 as compared against
655 measurements for the three selected regions given in µg/m^3. The corresponding regional statistics are provided in

 Table 7. Site locations and observed values, taken from the EMEP, CASTNET and EANET networks respectively,
657   are shown in circles.

658

659

660

661   **Table 7**: As for Table 3 except for NO_3^-.

	Europe (EMEP)		US (CASTNET)		SE Asia (EANET)	
NO_3^-	Cy48r1	pre-Cy49r1	Cy48r1	pre-Cy49r1	Cy48r1	pre-Cy49r1
MB ($\mu g/m^3$)	0.95	0.10 (-90)	1.71	0.10 (-94)	2.68	-0.16 (-94)
RMSE	2.37	1.60 (-32)	2.20	0.83 (-62)	3.62	1.41 (-61)
Pearsons R	0.41	0.58 (+29)	0.31	0.57 (+46)	0.65	0.52 (-20)

662

663   **5 The changes in regional wet deposition**

664

665   In this section, we evaluate the temporal distribution and biases associated with the yearly wet deposition terms of
666   soluble trace gas species and particulates. All three SIA are lost to the surface by both dry and wet deposition
667   processes. Over the last decades the main source of acidification has shifted from SO_x based to NO_x based in line
668   with the reduction measures imposed for SO_x and the increase and associated emission changes from e.g. road
669   transport. Here we evaluate whether pre-Cy49r1 captures the correct wet scavenging and improves on the
670   performance of Cy48r1 for the various dissolved precursors and SIA. Evaluations are made using comparisons of
671   model output against yearly wet deposition totals as taken from the observational networks introduced in Sect. 3.
672   The concentrations of the dissolved precursors (i.e. SO_2(aq), NH_3(aq) and HNO_3(aq)) also undergo wet deposition
673   (in IFS-COMPO) and cannot be differentiated well in the observational networks and are therefore included in the
674   measured totals. The wet deposition term is also influenced by meteorological parameters such as the simulated
675   large-scale and convective mixing, liquid and solid precipitation droplet size, SAD, and the frequency and intensity
676   of precipitation as provided by the IFS model.

677   The changes in the global tropospheric burden, lifetime, dry and wet deposition totals for SO_4^{2-}, NH_4^+, NO_3^- (fine)
678   and NO_3^- (coarse) during 2018 are given in Table 8. The corresponding statistics for the changes in wet deposition
679   between Cy48r1 and pre-Cy49r1 as compared against yearly observational means yearly for SO_x, reduced N and
680   oxidised N are provided for the three chosen global regions in Table 9.

681   **Table 8**: The global budget values for the burden, tropospheric lifetime, wet and dry deposition
682   terms for SO_4^{2-}, NH_4^+ and NO_3^- for 2018. Totals are provided in Tg S/year and Tg N/year. Percentage
683   difference changes are calculated as ((pre-Cy49r1-Cy48r1)/Cy48r1) *100 and given in parentheses.

	Cy48r1	pre-Cy49r1_NOE4C	pre-Cy49r1
SO_4^{2-}			
Burden	0.4	0.6 (+30)	0.6 (+30)
Lifetime (days)	3.4	4.4 (+29)	4.4 (+29)
Dry dep	5.8	5.4 (-7)	5.4 (-7)
Wet dep	43.1	43.9 (+2)	44.2 (+3)
NH_4^+			
Burden	0.3	0.4 (+32)	0.2 (-33)

	Cy48r1	pre-Cy49r1_NOE4C	pre-Cy49r1
Lifetime (days)	3.5	4.6 (+34)	4.1 (+18)
Dry dep	5.1	5.1 (-)	1.8 (-64)
Wet dep	27.5	27.1 (-2)	20.1 (-40)
NO_3^- (fine)			
Burden	0.01	0.01 (-)	0.02 (+86)
Lifetime (days)	4.9	5.4 (+12)	6.1 (+25)
Dry dep	0.2	0.2 (-21)	0.1 (-32)
Wet dep	0.6	0.5 (-13)	1.0 (+64)
NO_3^- (coarse)			
Burden	0.01	0.01 (-)	0.01 (-)
Lifetime (days)	3.4	3.8 (+11)	2.4 (-29)
Dry dep	1.5	2.5 (+73)	1.2 (-18)
Wet dep	3.5	2.8 (-20)	0.7 (-79)

684

685 **Table 9**: The yearly MB, RMSE and Pearsons R values for the comparisons of the yearly mean regional wet
686 deposition totals of dissolved $SO_2+SO_4^=$, $NH_3+NH_4^+$ and $HNO_3+NO_3^-$ as compared against composites assembled
687 from the regional observation networks for 2018 shown in Figures 9-11 for Europe, the U.S. and Southeast Asia.
688 Percentage difference changes are calculated as ((pre-cy49r1-Cy48r1)/Cy48r1) *100 and given in parentheses.

	Europe (EMEP)		US (CASTNET)		SE Asia (EANET)	
SO_X	Cy48r1	pre-Cy49r1	Cy48r1	pre-Cy49r1	Cy48r1	pre-Cy49r1
MB (mgS/m^2/yr)	-42	-38 (-9)	137	190 (+39)	-44.2	8.7 (-80)
RMSE	88.2	85 (-3)	203	270 (+33)	447	500.3 (+12)
Pearsons R	0.55	0.58 (+6)	0.68	0.66 (-3)	0.72	0.65 (-10)
Reduced N						
MB (mgN/m^2/yr)	61	25.9 (-58)	8.4	6.8 (-21)	12	-44 (+260)
RMSE	114	93.4 (-18)	76.0	81.3 (+7)	318	302 (-5)
Pearsons R	0.69	0.68 (-1.4)	0.77	0.72 (-16)	0.75	0.71 (-1)
Oxidised N						
MB (mgN/m^2/yr)	9.7	-1.4 (-86)	130	99.7 (-23)	142	98.3 (-31)
RMSE	69	72 (+4)	153	122.6 (-20)	324	274.3 (-15)
Pearsons R	0.50	0.47 (-6)	0.86	0.85 (-1)	0.67	0.68 (+2)

689

5.1 Total yearly wet S deposition

690

691 Figure 10 shows the regional distribution and values of yearly wet S deposition for Europe, the U.S., and Southeast
692 Asia in both Cy48r1 and pre-Cy49r1 during 2018. To allow a direct comparison across regions we use a colour
693 scale which covers values larger than 500 mgS/m^2/year in Southeast Asia. The global budget terms for SO_4^{2-} are
694 presented in Table 8 and show that, despite the global burden increasing by one third, only very small increases of
695 a few percent occur in the yearly wet SO_4^{2-} totals (Rémy et al., 2024), with associated decreases in the dry
696 deposition term. The significant increase in the tropospheric SO_4^{2-} lifetime means more remains in the aerosol

697 phase and will increase both AOD and the degree of scattering in IFS-COMPO as shown for AOD comparisons
698 in Rémy et al. (2024). The most significant change is in the direct gas-phase production term of $H_2SO_4(g)$, where
699 increases in $[SO_2(g)]$ subsequently increase the total mass scavenged into aqueous cloud droplets. This results in
700 an extent of acidification (slowing in-situ oxidation; c.f. Table 2), which is buffered by the increased phase transfer
701 of $NH_3(g)$ (c.f. Table 4). These changes are the result of updates to the scavenging approach rather than the
702 application of EQSAM4Clim. Although there is a 16% reduction in the total global $SO_2(aq)$ wet deposition (c.f.
703 Table 2), this is compensated for by increases in $[SO_4^{2-}(aq)]$ which results in an increase in the cumulative wet S
704 deposition yearly totals.

705 For Europe (top panels), the changes between model simulations are like the changes in the $SO_2(g)$ and SO_4^{2-}
706 particle concentrations discussed in Sect. 4. Compared against the yearly mean observational values from EMEP,
707 which range from 100-500 mgS/m²/year, there is an underestimation in Cy48r1 of approximately 100 mgS/m²/year
708 for northwest Europe. For the observational means in Ireland, Poland, northern Spain and on the Iberian Peninsula
709 negative MB are enhanced to around 300 mgS/m2/year. This indicates missing local source terms in the global
710 emission inventory provided as monthly mean fluxes. For other regions, the agreement is satisfactory capturing
711 the observed deposition gradient from Germany into Austria/northern Italy. For pre-Cy49r1, strong similarity
712 exists for Benelux, Denmark, and Italy, where negative biases of around 50-100 mgS/m²/year occur. A significant
713 negative yearly MB exists in Europe, which decreases by around 10% in pre-Cy49r1 (c.f. Table 9) with a marginal
714 increase in the correlation. Considering the associated positive MB for aerosol SO_4^{2-} shown during summertime
715 (c.f. Figure 2), there is an indication that not enough phase transfer occurs, thus negative MB values for the yearly
716 deposition totals, and the large observational means at selected stations influencing the regional yearly mean.

717 For the U.S. (middle panels) there is a stark contrast to the changes shown for Europe. Analysis of the yearly
718 observational yearly mean values from CASTNET shows that a gradient exists in the wet deposition yearly totals
719 from east to west, similar to that for $SO_2(g)$ and the location of primary SO_2 emission sources (c.f. Fig. 1). Maximal
720 values of 300-400 mgS/m²/year occur towards the east coast where a positive MB occurs for $[SO_4^{2-}]$ (c.f. Fig. 3).
721 For Cy48r1, this gradient in yearly wet deposition is captured to a large degree, albeit with significant positive
722 biases of > 100 mgS/m²/year with a maximal range of 700-900 mgS/m²/year. There is a significant yearly wet
723 deposition of SO_x in the Atlantic (250-400 mgS/m²/year) due to the local oxidation of DMS (released from the
724 ocean) and the long-range transport of $SO_2(g)/SO_4^{2-}$ from the anthropogenic source regions. In pre-Cy49r1 the area
725 of maximal wet S deposition increases around, e.g., New York state extending south to Texas resulting in an
726 increase in the positive yearly MB for the U.S. by nearly 40% (to 190 mgS/m²/year). This contrasts with the
727 significant improvement in the yearly MB for $[SO_4^{2-}]$ given in Table 3, which provides the continental mean rather
728 than statistics for the east coast. The changes are determined by changes in the scavenging of SO_4^{2-} particles into
729 the aqueous phase, with the application of EQSAM4Clim having a minor influence (Table 8).

730 Finally for Southeast Asia (bottom panels), the magnitude of EANET yearly wet depositional totals show that
731 more than twice the amount of S deposition occurs as measured in either Europe or the U.S. over an identical
732 period and a much wider area, reaching 1200-1300 mgS/m²/year in central and eastern China (not shown). The
733 spatial distribution of stations shows that a negative gradient exists between deposition totals in China and those
734 extending towards Myanmar (west) and Japan (east) (2000-2200 mgS/m²/year; not shown). This indicates the
735 importance of the transport component of SO_4^{2-} when considering the low regional $SO_2(g)$ precursor mixing ratios
736 around the equator (c.f. Fig. 1), and that the primary sources are typically infrequent volcanic eruptions for the
737 region between 5°N-5°S (Fioletov et al., 2020) that typically inject the SO_2 above the boundary layer (thus with a
738 limited impact on the surface values). Towards the coast of eastern China and Japan, the observations show yearly
739 totals of 250-350 mgS/m²/year, in contrast to high values near the middle of China. Such local scale variability is
740 not captured using the current emission inventory that is employed, where the positive MB increases significantly
741 in pre-Cy49r1 using the same observational stations and emission estimates (c.f. Table 3). The extent of high wet
742 deposition values reaches hundreds of kilometres from the coast far away from prescribed emission sources. The
743 regional yearly MB improves markedly to 8.7 mgS/m²/year in pre-Cy49r1 despite increases in the MB and
744 decreases in the Pearson's R value for $[SO_4^{2-}]$ (Table 3).
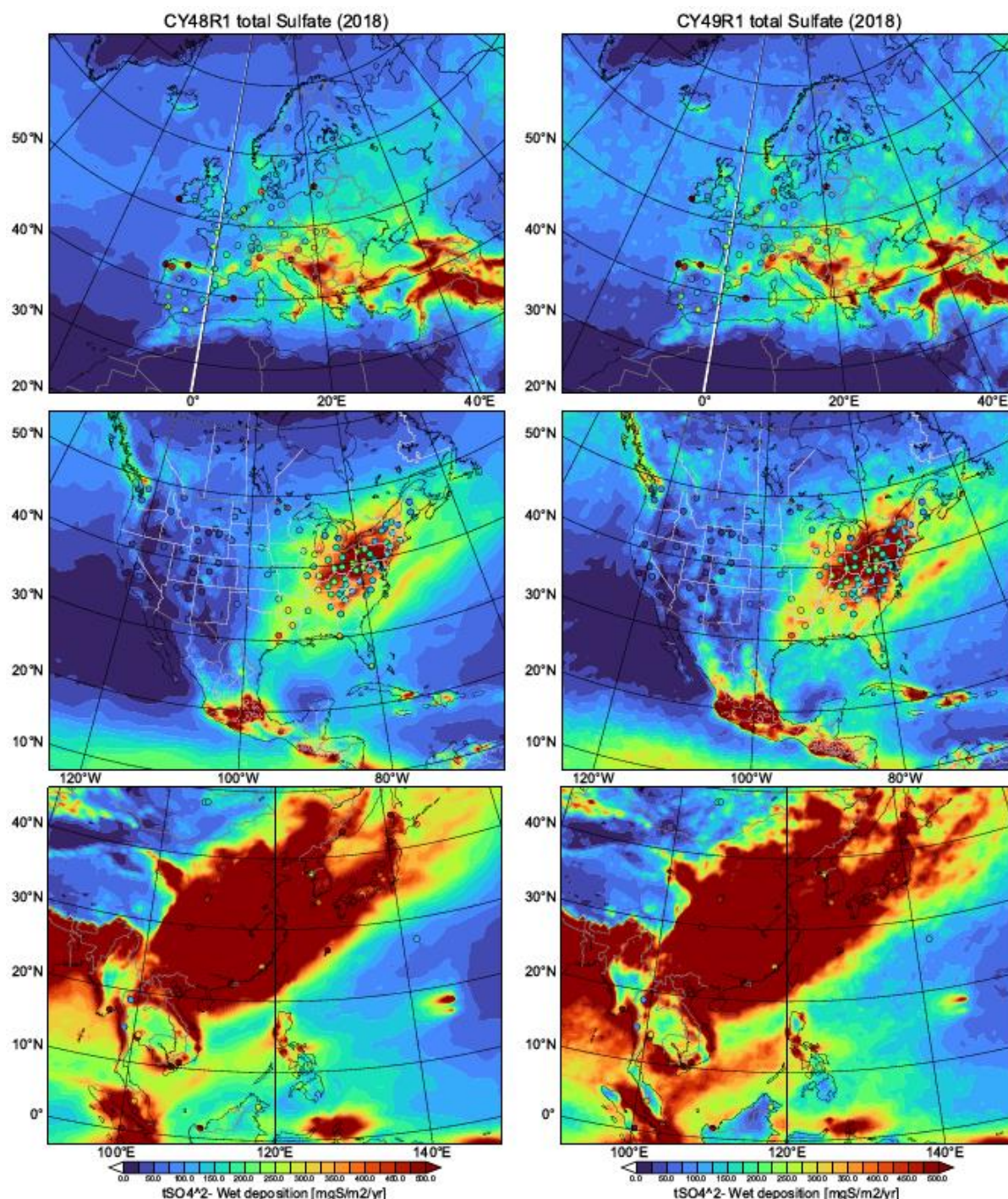
Figure 10: Yearly comparisons of the cumulative wet deposition totals of dissolved SO_2 and SO_4^{2-} aerosol (mgS/m^2/year) for 2018 as simulated in Cy48r1 (left column) and pre-Cy49r1 (right column) shown for Europe (top), the U.S. (middle) and Southeast Asia (bottom). The corresponding statistics are provided in Table 9. Site locations and observed values, taken from the EMEP, CASTNET and EANET networks respectively, are shown in circles.

5.2 Total yearly wet NH$_x$ deposition

In Figure 11 we show the corresponding changes in the total yearly mean wet deposition of reduced N for both Cy48r1 and pre-Cy49r1 during 2018 for the three global regions. The location of the sampling stations is identical to those shown above for the wet S deposition evaluation. In Table 8, the global chemical budget terms for NH_4^+ show that for pre-Cy49r1_NOE4C there is an increase the tropospheric burden by one third (as for SO_4^{2-}, with $(NH_4)_2SO_4$ being a dominant SIA, Seinfeld and Pandis, 2006). This is subsequently reversed when applying

757   EQSAM4Clim in pre-Cy49r1 This results in significant decreases in both the total yearly global dry and wet
758   deposition terms for reduced N (> 50% from Table 8).

759   For Europe (top panels), where high summertime NH_3(g) mixing ratios are simulated (c.f. Fig. 4 in Sect. 4), the
760   EMEP observational yearly wet deposition totals show that peak values exist in the Balkans, Germany, Austria
761   and northern Italy (Po valley), and that local regional variability exists in e.g. France (ranging between 250-350
762   mgN/m^2/year). For regions with low NH_3 emissions, such as Scandinavia and the Iberian Peninsula, wet deposition
763   totals generally have a lower range, of between 50-200 mgN/m^2/year. For Cy48r1, the high resident surface mixing
764   ratios of NH_3(g) (5-15 ppb; Fig. 1) results in a relatively high NH_x yearly total wet deposition values of between
765   350-500 mgN/m^2/year for northwest and central Europe at a country-wide scale (e.g. the Netherlands and
766   Belgium). Measured yearly mean values from EMEP are typically exceeded, which results in a yearly MB of 61
767   mgN/m^2/year in Cy48r1, albeit with a high correlation of 0.69 (c.f. Table 8), reflecting the positive local MB
768   shown for $[NH_4^+]$ shown in Fig. 6. Comparing the yearly mean temporal distribution simulated in pre-Cy49r1
769   shows a significant reduction in the area with maximal values (> 450 mgN/m^2/year), being limited to northern
770   Italy only. The reduction in $[NH_4^+]$ (c.f. Table 4) reduces the yearly MB in wet deposition by nearly 60%, without
771   any notable degradation in the correlation coefficient. Thus, the application of EQSAM4Clim significantly
772   improves the simulation of reduced N wet deposition in IFS-COMPO for Europe.

773   For the U.S. (middle panels), the AMoN observations show that there is a similar east-west gradient in the total
774   reduced N wet deposition totals as that for NH_3(g) surface mixing ratios and $[NH_4^+]$ distributions (c.f. Fig. 4 and
775   6, respectively). The range in observed total wet deposition values is between 30-400 mgN/m^2/year showing that,
776   in the absence of local NH_3 emission sources, that levels of deposition are low (lower than that observed for
777   Europe). Comparing the temporal distribution of reduced N wet deposition in Cy48r1 shows that the continental
778   gradient is captured, although maximal values which occur towards central U.S. are not seen in the measurements
779   (>100% MB) being influenced by the high local NH_3 emission flux. For the east coast, where most primary NH_3
780   sources are located, there is generally an overestimation in the wet deposition simulated in Cy48r1. Compared to
781   Europe, the yearly MB for the U.S. is low at 9 mgN/m^2/year in Cy48r1. This is a result of the large positive MB
782   towards the east being moderated by negative in other parts of the U.S. There is an improvement in the MB in pre-
783   Cy49r1, albeit with a degradation in the Pearsons' R to 0.72.

784   For Southeast Asia, the EANET observational yearly mean wet deposition totals show that, similar to that shown
785   for S deposition, much higher values occur than for the other two regions presented. The yearly deposition values
786   range between 200-2400 mgN/m^2/year (not shown), with the highest measured values occurring more inland and
787   away from coastal regions. The simulated temporal distribution in wet reduced N deposition does capture the
788   variability across individual stations quite well across a wide area (c.f. from China to Japan). In Cy48r1, the yearly
789   MB is 12 mgN/m^2/year on high yearly totals resulting in it being the lowest for all the regions, with a high
790   correlation coefficient of 0.75. For pre-Cy49r1, there is a larger negative MB (although still relatively small
791   compared to the large totals), in-spite of the lower (positive) MB simulated for the $[NH_4^+]$ comparisons as
792   compared to Cy48r1 (c.f. Table 5), again with a modest degradation in the correlation.
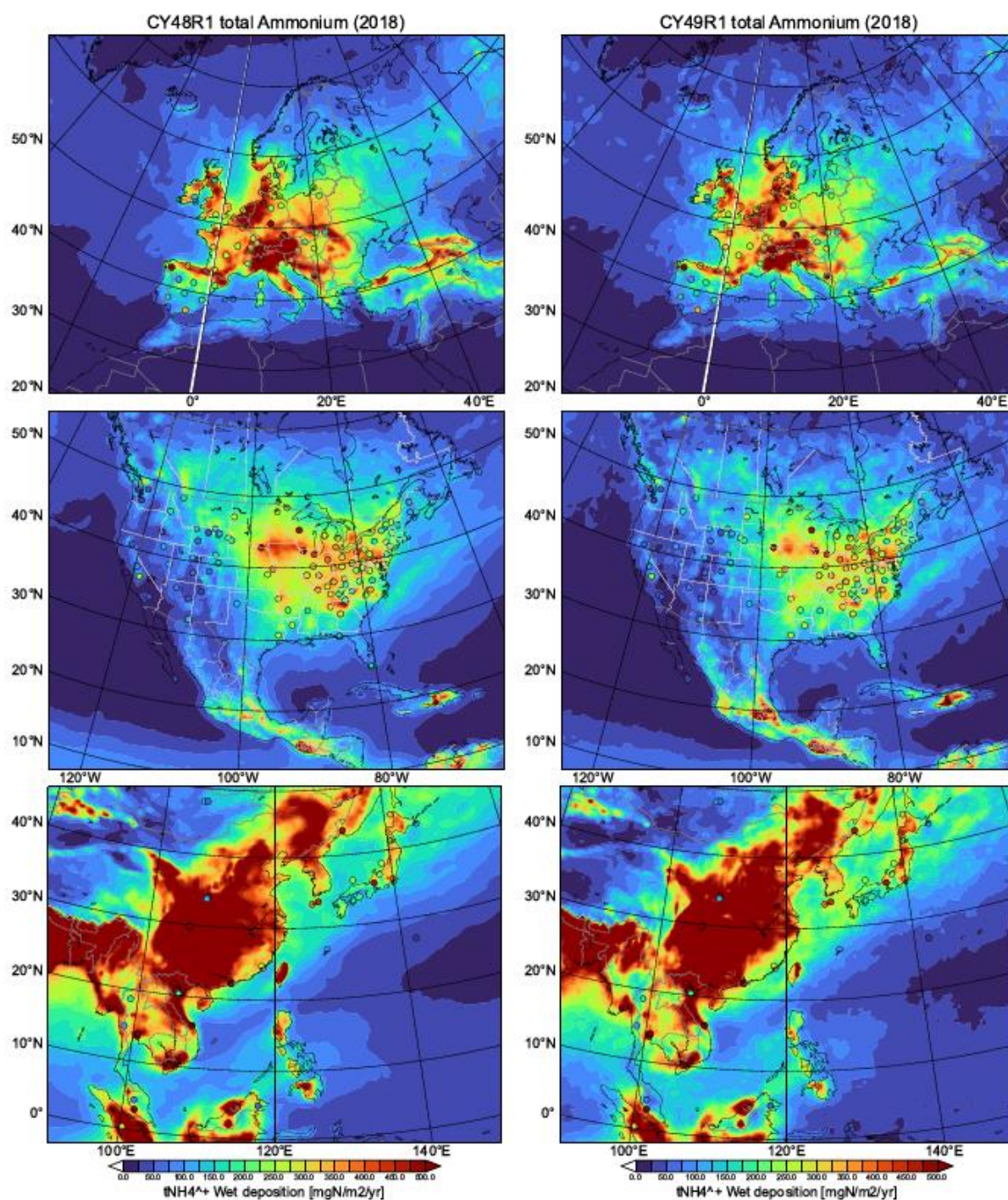
Figure 11: Yearly comparisons of the cumulative wet deposition totals of dissolved NH_3 and NH_4^+ aerosol (mgN/m^2/year) for 2018 as simulated in Cy48r1 (left column) and pre-Cy49r1 (right column) shown for Europe (top), the U.S. (middle) and Southeast Asia (bottom). The corresponding statistics are provided in Table 9. Site locations and observed values, taken from the EMEP, CASTNET and EANET networks respectively, are shown in circles.

5.3 Total yearly wet NOx deposition
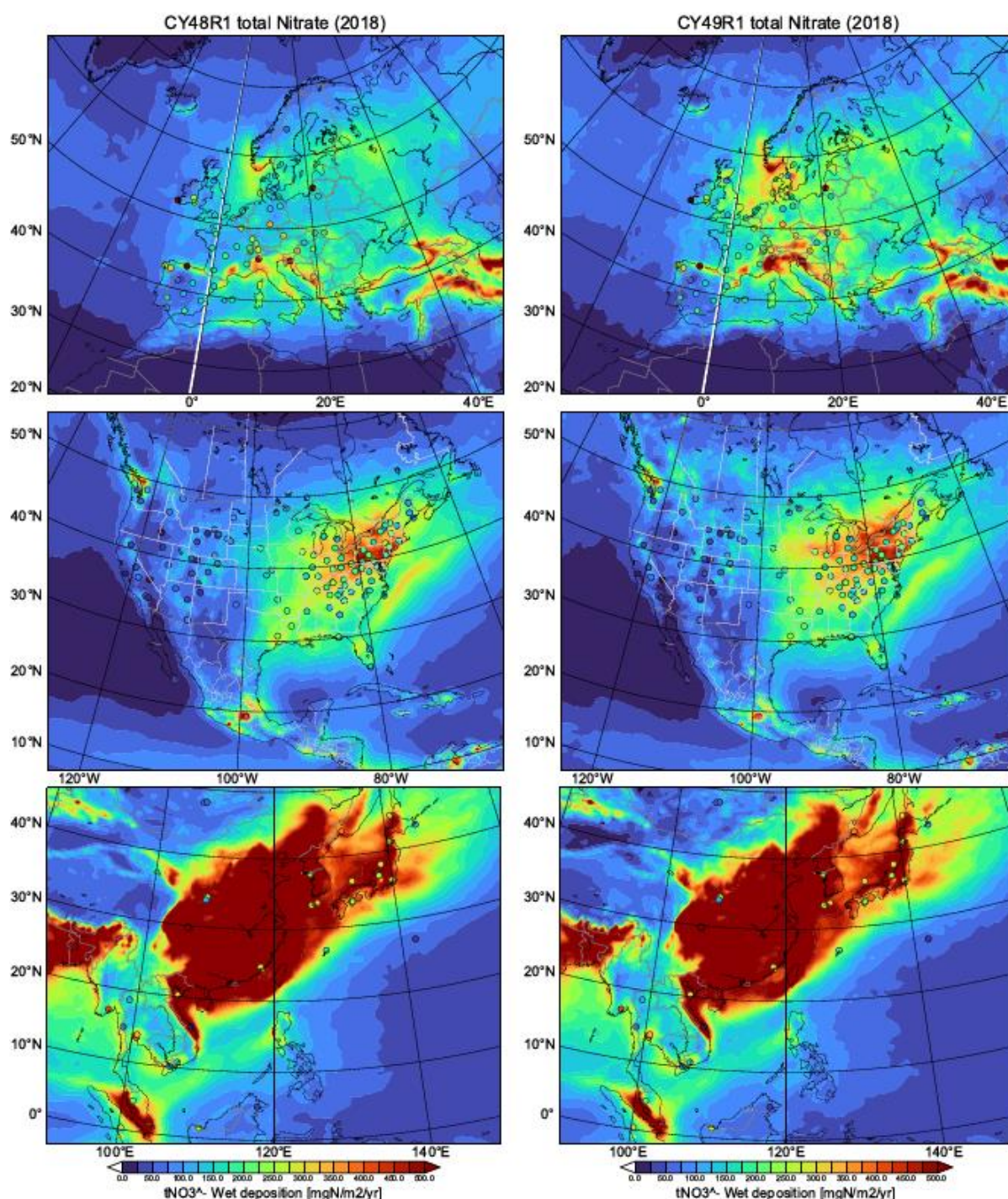
804
Figure 12: Yearly comparisons of the cumulative wet deposition totals of dissolved HNO_3 and NO_3^- aerosol
(mgN/m^2/year) for 2018 as simulated in Cy48r1 (left column) and pre-Cy49r1 (right column) shown for Europe
(top), the U.S. (middle) and Southeast Asia (bottom). The corresponding statistics are provided in Table 9. Site
locations and observed values, taken from the EMEP, CASTNET and EANET networks respectively, are shown
in circles.

Finally, in Figure 12 the corresponding changes in the total yearly mean wet deposition of oxidised N for both
Cy48r1 and pre-Cy49r1 during 2018 are shown. The global chemical budget terms provided in Table 6 reveal that
there is an increase in the gas-phase production term for HNO_3, with a relatively constant heterogeneous
conversion term for N_2O_5 when summed over the various reactive surfaces. Once formed, a significant fraction of
HNO_3 is directly scavenged into aqueous cloud droplets and deposited to the surface as wet (acidic) deposition
(c.f. Rémy et al, 2024). However, the large biases shown for $HNO_3(g)$ do reveal a limit to the loss via wet

816 scavenging and deposition, with an excess remaining in the gas phase, which impacts the results shown in this
817 section. Note that the particulate NO_3^- takes various chemical forms in IFS-COMPO ($Ca(NO_3)_2$, $NaNO_3$, KNO_3,
818 NH_4NO_3), therefore there is only partial commonality between the changes shown for NH_4^+ and NO_3^-. With the
819 application of EQSAM4Clim in pre-Cy49r1, the surface concentration and burden of NH_4^+ decreases strongly,
820 while the gas phase concentration of HNO_3 increases (c.f Table 4 and 6; Figs. 5 and 8).

821 For Europe (top panels), the observational yearly total wet deposition values from EMEP show that there is a rather
822 constrained range in the deposition of total oxidised N deposition (150-275 mgN/m^2/year) apart from a few outliers
823 such as on the southern coast of Ireland which have values > 500 mgN/ m^2/year. In general, there are increases in
824 the yearly wet deposition of [NO_3^-] between Cy48r1 and pre-Cy49r1, which increases the regional background
825 totals improving agreement in e.g. Germany, which significantly reduces the yearly MB (c.f. Table 9). In contrast
826 to oxidized S, pre-Cy49r1_NOE4C simulates a reduction in the yearly wet deposition totals, for oxidized N which
827 is further decreased for the coarse mode by applying EQSAM4Clim. The increase in [$HNO_3(g)$] means a larger
828 fraction of oxidized N remains in the gas-phase thus reducing [NO_3^-] and improving the MB against observations
829 as shown in Sect. 4. This subsequently leads to an improvement in performance for the regional yearly wet
830 deposition totals. However, the large significant MB introduced for [$HNO_3(g)$] shows that another loss term is
831 necessary for fully describe the budget of oxidized N across phases. For the U.S. (middle panels), higher values of
832 oxidised N deposition occur towards the east coast as defined by the distribution of NO_x emissions (Figs. 12). The
833 range in the observational total wet deposition values from CASTNET is between 50-500 mgN/m^2/year, exhibiting
834 a strong longitudinal gradient. Although this gradient is captured rather well, there is typically an overestimation
835 of between 100-200 mgN/m^2/year for e.g. New York state and the surrounding regions in Cy48r1. For the Western
836 U.S., observations provide the range of between 0-100 mgN/m^2/year, with positive model biases of 100
837 mgN/m^2/year for the northwestern states in both model versions. For the southern U.S., Cy48r1 exhibits
838 overestimates of 50-70 mgN/m^2/year, which decreases noticeably in pre-Cy49r1. There is a large positive MB in
839 Cy48r1 of 130 mgN/m^2/year which is improved in pre-Cy49r1 decreasing by 23%. Again, the Pearsons R value
840 remains relatively unaffected showing the governing influence of the spatial distribution of the main point sources.

841 For Southeast Asia (bottom panels), the range in the EANET observational total wet deposition values is between
842 50-800 mgN/m^2/year (not shown), with the highest values of >2000 mgN/m^2/year occurring on the Malaysian
843 Coast. For northern and central China, total wet deposition values of up to 500 mgN/m^2/year occur, covering a
844 wide area including the similar to oxidised S. For Cy48r1, simulated values exceed observed values by 100-400%,
845 with a lack of spatial variability across the domain. Much better agreement occurs for Mynmar, Cambodia and
846 Thailand related to much lower NOx emissions. Comparing Cy48r1 and pre-Cy49r1 shows that a marked decrease
847 in the MB of 31% occurs between cycles, although the MB is at least twice that simulated for the other continents.

848 **6 Conclusions**
849

850 In this paper we build on the previous evaluations of the performance of IFS-COMPO pre-Cy49r1 presented in
851 Rémy et al. (2024), and quantify the impact of applying the EQSAM4Clim module in IFS-COMPO for the revised
852 calculation of aerosol and cloud pH (Metzger et al., 2024) on its ability to improve air quality forecasts of SIA. To
853 scrutinise its effect on atmospheric composition, we have compared an operational IFS version (Cy48r1) with the
854 next operational IFS version, which uses EQSAM4Clim in combination with a unified wet scavenging approach
855 and other developments (pre-Cy49r1). Further improvements are also made with respect to both in-cloud and
856 below cloud scavenging of soluble trace gases and aerosols through an implementation of updated
857 parameterizations as detailed in Rémy et al. (2024).

858 EQSAM4Clim significantly influences wet deposition processes through its impact on aerosol loading and gas-
859 aerosol partitioning. By altering the aerosol and cloud pH, the scheme modulates the chemical oxidation rates of
860 precursor gases such as NH_3, SO_2 and HNO_3. This, in turn, affects the formation and partitioning of SIA, their
861 hygroscopic growth, and their subsequent removal of both dry and wet deposition pathways - including in-cloud
862 and below-cloud scavenging. These changes also influence the aerosol radiative effects, both directly and
863 indirectly, underscoring the interconnected role of thermodynamic aerosol modeling in atmospheric composition
864 and deposition simulations.

865 When applying EQSAM4Clim in a large-scale high resolution global modelling framework, we have shown that
866 the most significant impacts of our IFS-COMPO updates concern the production efficacy of SIA and subsequent
867 phase partitioning of reduced/oxidised nitrogen species. Comparing simulations with and without EQSAM4Clim,
868 shows that changes in SIA are principally caused by altering the gas/aerosol partitioning as predicted. The gaseous
869 precursors, SIA surface concentrations and wet deposition totals for the three dominant global source regions

870 (Europe, the U.S., and Southeast Asia) have been evaluated against weekly/yearly observational composites for
871 2018.

872 For $SO_2(g)/SO_4^{2-}$, the conversion rate only exhibits moderate changes, with statistics being strongly impacted by
873 the emission inventory employed. For $SO_2(g)$, an increase in the global tropospheric burden of 7% shows less
874 phase transfer due to limitations in the uptake imposed by the increase in the pH of the solution. An increase in
875 the gas phase production term of $H_2SO_4(g)$, which is subsequently scavenged, offsets a modest reduction in the
876 aqueous phase production term of 2%. For surface $[SO_2(g)]$, no significant impact has occurred with respect to the
877 mean bias against observational means in Europe and the U.S. . Moreover, the correlation in the weekly variability
878 improves only marginally. For $[SO_4^{2-}]$ there is an increase in both the tropospheric burden and lifetime by one
879 third due to the wet scavenging updates made to IFS-COMPO, with an associated reduction in the yearly mean
880 biases for Europe and the U.S. and increases in the corresponding correlation coefficients. However, for China
881 there is a degradation in the performance which is associated with an increase in the positive yearly mean bias and
882 a decrease in the correlation coefficient. For the wet deposition of oxidized S, results are mixed. Reductions in the
883 mean bias are found for Europe and China, whilst for the U. S. the MB increases markedly.

884 For $NH_3(g)/NH_4^+$ the changes from applying EQSAM4Clim online are substantial, resulting in beneficial
885 improvements in the global modelling of reduced nitrogen. For $NH_3(g)$ the tropospheric burden almost doubles
886 due to a halving of the conversion rate of $NH_3(g)$ into NH_4^+, where more $NH_3(g)$ is directly deposited to the surface.
887 For surface $[NH_3(g)]$, there is some similarity in the increases in the weekly mean bias between Europe and the
888 U.S. For $[NH_4^+]$, the application of EQSAM4Clim significantly reduces the associated mean bias against
889 observational yearly means by approximately 45% for all three global regions. This is explained by a reduction in
890 the efficacy of particle formation, especially during summertime. For the yearly wet deposition component, the
891 positive mean bias almost halves for Europe and the U.S., whilst increasing significantly for Southeast Asia.

892 For $HNO_3(g)/NO_3^-$ the changes due to EQSAM4Clim are similar to those simulated for the $NH_3(g)/NH_4^+$
893 partitioning due to the speciation of the SIA being mainly linked via NH_4NO_3. The gas-phase production of
894 $HNO_3(g)$ increases by 15-20% with a limited increase in the global tropospheric burden of 3% due to compensating
895 increases in the loss to surface via both dry and wet deposition. The application of EQSAM4Clim increases the
896 fine aerosol component whilst reducing the coarse aerosol component, which reduces the fraction of $HNO_3(g)$ held
897 in the particulate phase by 50% and increases transport lifetimes for smaller particles. For $HNO_3(g)$ in Europe,
898 there is a persistent negative bias during the summertime which is changed to a significant positive mean bias due
899 to a larger fraction remaining in the gas phase. For the U. S., there is a degradation with a relatively low mean bias
900 changing to a large positive bias for the entire year which indicates an incomplete process coupling when
901 considering mineral cations without aerosol dynamics. For $[NO_3^-]$, significant improvements in the yearly mean
902 biases occur across the globe as illustrated by the three chosen regions, which comes with improvements in the
903 simulated correlation coefficients. For the yearly wet deposition totals, there are reductions in the mean bias for
904 all regions, without any significant change in the correlation.

905 In summary, although the impact on $SO_2(g)/SO_4^{2-}$ are rather small across various global regions, the impact on
906 both particle concentrations and wet deposition totals for both reduced and oxidised N improve markedly for both
907 Europe and the U.S., whereas for Southeast Asia changes are rather mixed. Significant improvements could be
908 made by applying more accurate emission inventories and including additional anions such as chlorine from sea-
909 salt to influence coastal regions and the significant changes simulated over the oceans in this study. Overall, the
910 recent improvements brought by EQSAM4Clim (Metzger et al., 2024) as applied here and in Rémy et al. (2024),
911 shows that the changes shown for pre-Cy49r1 are fit-for-purpose with respect to capturing regional particle
912 concentration and the loss terms via wet deposition and improve the forecasting on PM at global scale.

913

914 **Appendix**
915

916
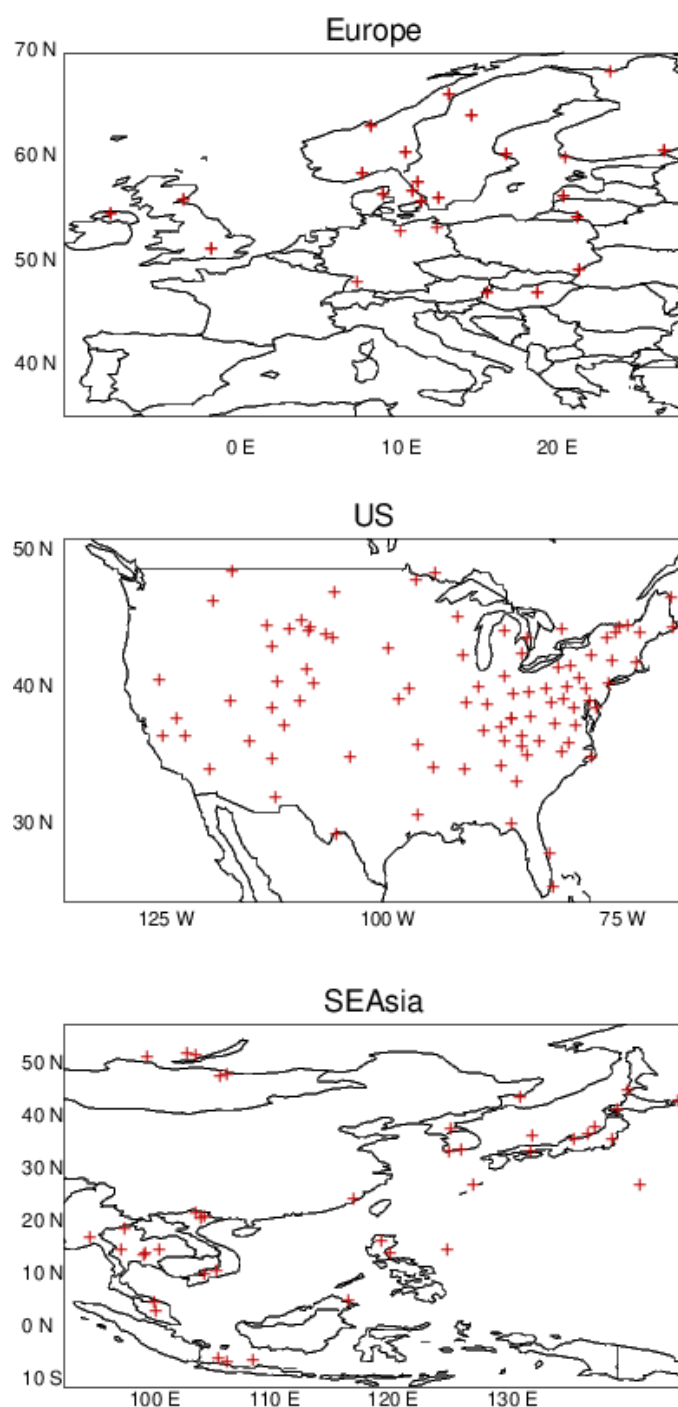
Figure A1: The location of the observational sites used for evaluating the
surface concentration of SO_2 for Europe (top panel), the U.S. (middle panel)
and SEAsia (lower panel).

917
918
919

920 ***Author Contributions***
921 JEW and SM were principal authors of the paper and produced most of the figures. SR conducted the IFS-COMPO
922 simulations and performed the regional comparisons made against observational datasets for evaluating the
923 deposition fluxes and was a co-PI of the CAMS35_2 development project. SM provided EQSAM4Clim for the
924 more accurate calculation of pH using aerosols and clouds, which the authors have integrated into IFS-COMPO.
925 VH updated the model towards pre-Cy49r1, introduced technical updates with respect to the implementation of
926 EQSAM4Clim and was co-PI of the CAMS35_2 development project. JF is a representative of the CAMS
927 consortium under which this work was conducted.

928 *Code availability*

929 Model codes developed at ECMWF are the intellectual property of ECMWF and its member states, and therefore
930 the IFS code is not publicly available. ECMWF member-state weather services and their approved partners will
931 get access granted. Access to a version of the IFS (OpenIFS) that includes this experimental cycle may be obtained
932 from ECMWF under an OpenIFS licence. More details at https://confluence.ecmwf.int/
933 display/OIFS/About+OpenIFS. A full description of Cy49r1 can be found here:
934 https://www.ecmwf.int/en/elibrary/81630-ifs-documentation-cy49r1-part-viii-atmospheric-composition.

935 *Data availability*

936 The surface data for IFS-COMPO used for this study is available on Zenodo
937 (https://doi.org/10.5281/zenodo.13902673).

938 *Competing Interests*

939 The main author and one of the co-authors are members of the editorial board of Geoscientific Model
940 Development. The peer-review process was guided by an independent editor, and the authors also have no other
941 competing interests to declare.

942 *Acknowledgements*

943 We acknowledge funding from the Copernicus Atmosphere Monitoring Service (CAMS), which is funded by the
944 European Union's Copernicus Programme. We acknowledge the EMEP, EANET, AirNow, CASTNET, AMoN,
945 AQeR and CNEMC monitoring networks for allowing access to surface observational data for the pre-cursor gases
946 and associated particulates.

947

References

949

950 van der A, R. J., Ding, J., and Eskes, H.: Monitoring European anthropogenic NO_x emissions from space, Atmos.
951 Chem. Phys., 24, 7523–7534, https://doi.org/10.5194/acp-24-7523-2024 , 2024.

952 Aas, W., Mortier, A., Bowersox, V. *et al.* Global and regional trends of atmospheric sulfur. *Sci Rep* 9, 953,
953 https://doi.org/10.1038/s41598-018-37304-0, 2019.

954
955 Aas, W., Fagerli, H., Alastuey, A., Cavalli, F., Degorska, A., Feigenspan, S., Brenna, H., Gliß, J., Heinesen, D.,
956 Hueglin, C., Holubová, A., Jaffrezo, J.L., Mortier, A., Murovec, M., Putaud, J.P., Rüdiger, J., Simpson, D.,
957 Solberg, S., Tsyro, S., Tørseth, K. and Yttri, K.E. : Trends in Air Pollution in Europe, 2000–2019. Aerosol Air
958 Qual. Res. 24, 230237. https://doi.org/10.4209/aaqr.230237, 2024.

959
960 Andres, R. J. and Kasgnoc, A. D.: A time-averaged inventory of subaerial volcanic sulphur emissions, J. Geophys.
961 Res., 103(D19), 25251-25261, https://doi.org/10.1029/98JD02091, 1998.

962
963 Ault, A.P: Aerosol Acidity: Novel Measurements and Implications for Atmospheric Chemistry, *Acc. Chem. Res*,
964 53, 9, 1703–1714, https://doi.org/10.1021/acs.accounts.0c00303, 2020.

965 Benish, S. E., Bash, J. O., Foley, K. M., Appel, K. W., Hogrefe, C., Gilliam, R., and Pouliot, G.: Long-term
966 regional trends of nitrogen and sulfur deposition in the United States from 2002 to 2017, Atmos. Chem. Phys., 22,
967 12749–12767, https://doi.org/10.5194/acp-22-12749-2022, 2022.

968 Celik, S., Drewnick, F., Fachinger, F., Brooks, J., Darbyshire, E., Coe, H., Paris, J.-D., Eger, P. G., Schuladen, J.,
969 Tadic, I., Friedrich, N., Dienhart, D., Hottmann, B., Fischer, H., Crowley, J. N., Harder, H., and Borrmann, S.:
970 Influence of vessel characteristics and atmospheric processes on the gas and particle phase of ship emission
971 plumes: in situ measurements in the Mediterranean Sea and around the Arabian Peninsula, Atmos. Chem. Phys.,
972 20, 4713–4734, https://doi.org/10.5194/acp-20-4713-2020 , 2020.

973 Chang, C.-T., Wang, L., Wang L-J, Liu, C-P, Yang, C-J, Huang, J-C., Wang, C-P, Lin N-H. and Lin, T-C.: On the
974 seasonality of long-range transport of acidic pollutants in East Asia, Environ.Res.Letts., 17(9), doi:10.1088/1748-
975 9326/ac8b99, 2022.

976 Chen J, Cheng M, Krol M, de Vries W, Zhu Q, Liu X, Zhang F and Xu W (2023), Trends in anthropogenic
977 ammonia emissions in China since 1980: A review of approaches and estimations. Front. Environ. Sci.
978 11:1133753, doi: 10.3389/fenvs.2023.1133753.

979 Croft, B., Lohmann, U., Martin, R. V., Stier, P., Wurzler, S., Feichter, J., Posselt, R., and Ferrachat, S.: Aerosol
980 size-dependent below-cloud scavenging by rain and snow in the ECHAM5-HAM, Atmos. Chem. Phys., 9, 4653–
981 4675, 2009.

982 de Bruine, M., Krol, M., van Noije, T., Le Sager, P., and Rockmann, T.: The impact of precipitation evaporation
983 on the atmospheric aerosol distribution in EC-Earth v3.2.0, Geosci. Model Dev., 11, 1443–1465, 2018.

984 Dentener, F., Drevet, J., Lamarque, J. F.,Bey, I., Eickhout, B., Fiore, A. M., Hauglustaine, D., Horowitz, L. W.,
985 Krol, M.,Kulshrestha, U. C., Lawrence, M., Galy-Lacaux, C., Rast, S., Shindell, D., Stevenson, D., Van Noije, T.,
986 Atherton, C., Bell, N., Bergman, D., Butler, T., Cofala, J., Collins, B., Doherty, R., Ellingsen, K., Galloway, J.,
987 Gauss, M., Montanaro, V., Muller, J. F., Pitari, G., Rodriguez, J.,Sand erson, M., Solmon, F., Strahan, S., Schultz,
988 M., Sudo, K., Szopa, S., and Wild, O.: Nitrogen and sulfur deposition on regional and global scales:A multimodel
989 evaluation, Global Biogeo. Cycles, 20, GB4003, doi:10.1029/2005GB002672, 2006.

990 Deschaseaux, E., O'Brien, J., Siboni, N., Petrou, K., and Seymour, J. R.: Shifts in dimethylated sulfur
991 concentrations and microbiome composition in the red-tide causing dinoflagellate *Alexandrium minutum* during a
992 simulated marine heatwave, Biogeosciences, 16, 4377–4391, https://doi.org/10.5194/bg-16-4377-2019 , 2019.

993 Ding, J., van der A, R., Eskes, H., Dammers, E., Shephard, M., Wichink Kruit, R., Guevara, M., and Tarrason, L.:
994 Ammonia emission estimates using CrIS satellite observations over Europe, EGUsphere [preprint],
995 https://doi.org/10.5194/egusphere-2024-1073 , 2024.

996 Du, H., Li, J., Wang, Z., Dao, X., Guo, S.,Wang, L., et al.: Effects of regional transport on haze in the NorthChina
997 Plain: Transport of precursors or secondary inorganic aerosols.Geophysical Research Letters, 47,e2020GL087461,
998 https://doi.org/10.1029/2020GL087461 ,2020.

999 Feick, G. and Hainer, R. M.: On the Thermal Decomposition of Ammonium Nitrate. Steady-state Reaction
1000 Temperatures and Reaction Rate*, J. Am. Chem. Soc.*, 76, 22, 5860–5863, https://doi.org/10.1021/ja01651a096,
1001 1954.

1002 Fioletov, V., McLinden, C. A., Griffin, D., Theys, N., Loyola, D. G., Hedelt, P., Krotkov, N. A., and Li, C.:
1003 Anthropogenic and volcanic point source SO_2 emissions derived from TROPOMI on board Sentinel-5 Precursor:
1004 first results, Atmos. Chem. Phys., 20, 5591–5607, https://doi.org/10.5194/acp-20-5591-2020 , 2020.

1005 Gao, J., Wei, Y., Guoliang, S., Yu, H., Zhang, Z., Song, S., Wang, W., Liang, D. and Feng, Y.: Roles of RH,
1006 aerosol pH and sources in concentrations of secondary inorganic aerosols, during different pollution periods, Atms.
1007 Environ., 241, 117770, https://doi.org/10.1016/j.atmosenv.2020.117770, 2020.

1008 Ge, Y., Heal, M. R., Stevenson, D. S., Wind, P., and Vieno, M.: Evaluation of global EMEP MSC-W (rv4.34)
1009 WRF (v3.9.1.1) model surface concentrations and wet deposition of reactive N and S with measurements, Geosci.
1010 Model Dev., 14, 7021–7046, https://doi.org/10.5194/gmd-14-7021-2021 , 2021.

1011 Giorgi, F. and Chameides, W. L.: Rainout lifetimes of highly soluble aerosols and gases as inferred from
1012 simulations with a general circulation model, *J. Geophys. Res.*, 91, 367–376, 1986.

1013 Goldberg, D. L., Anenberg, S. C., Kerr, G. H., Mohegh, A., Lu, Z., & Streets, D. G.: TROPOMI NO2 in the United
1014 States: A detailed look at the annual averages, weekly cycles, effects of temperature, and correlation with surface
1015 NO2 concentrations. Earth's Future, 9, e2020EF001665. https://doi.org/10.1029/2020EF001665. 2021.

1016 Gu, B., Ju, X., Chang, J., Ge, Y. and Vitousek, P. M.: Integrated reactive nitrogen budgets and future trends in
1017 China, PNAS, 112 (28) 8792-8797, https://doi.org/10.1073/pnas.1510211112, 2015.

Hauglustaine, D. A., Balkanski, Y., and Schulz, M.: A global model simulation of present and future nitrate aerosols and their direct radiative forcing of climate, Atmos. Chem. Phys., 14, 11031–11063, https://doi.org/10.5194/acp-14-11031-2014, 2014.

He, H., Liang., X.-Z. and Wuebbles, D.J.: Effects of emissions change, climate change and long-range transport on regional modeling of future U.S. particulate matter pollution and speciation, Atmos. Environ., 179, 166-176, https://doi.org/10.1016/j.atmosenv.2018.02.020, 2018.

Holland, E. A., Braswell, B. H., Lamarque, J.-F., et al.: Variations in the predicted spatial distribution of atmospheric nitrogen deposition and their impact on carbon uptake by terrestrial ecosystems, J. Geophys. Res., 102, 15 849–15 866, 1997.

Huijnen, V., Flemming, J., Chabrillat, S., Errera, Q., Christophe, Y., Blechschmidt, A.-M., Richter, A., and Eskes, H.: C-IFS-CB05-BASCOE: stratospheric chemistry in the Integrated Forecasting System of ECMWF, Geosci. Model Dev., 9, 3071–3091, https://doi.org/10.5194/gmd-9-3071-2016 , 2016.

Huijnen, V., Pozzer, A., Arteta, J., Brasseur, G., Bouarar, I., Chabrillat, S., Christophe, Y., Doumbia, T., Flemming, J., Guth, J., Josse, B., Karydis, V. A., Marécal, V., and Pelletier, S.: Quantifying uncertainties due to chemistry modelling – evaluation of tropospheric composition simulations in the CAMS model (cycle 43R1), Geosci. Model Dev., 12, 1725–1752, https://doi.org/10.5194/gmd-12-1725-2019, 2019.

Huijnen, V., Le Sager, P., Köhler, M. O., Carver, G., Rémy, S., Flemming, J., Chabrillat, S., Errera, Q., and van Noije, T.: OpenIFS/AC: atmospheric chemistry and aerosol in OpenIFS 43r3, Geosci. Model Dev., 15, 6221–6241, https://doi.org/10.5194/gmd-15-6221-2022 ,2022.

von Glasow, R., Lawrence, M. G., Sander, R., and Crutzen, P. J.: Modeling the chemical effects of ship exhaust in the cloud-free marine boundary layer, Atmos. Chem. Phys., 3, 233–250, https://doi.org/10.5194/acp-3-233-2003 , 2003.

Jayne, J. T., Davidovits, P., Worsnop, D. R., Zahniser, M. S., and Kolb, C. E.: Uptake of $SO_2(g)$ by Aqueous Surfaces as a Function of pH : The Effect of Chemical Reaction at the Interface, J. Phys. Chem., *J. Phys. Chem.*, 94, 15, 6041–6048, https://doi.org/10.1021/j100378a076, 1990.

Jiang, Z., Zhu, R., Miyazaki, K., McDonald, B. C., Klimont, Z., Zheng, B., et al.: Decadal variabilities in tropospheric nitrogen oxides over United States, Europe, and China. Journal of Geophysical Research: Atmospheres, 127, e2021JD035872. https://doi.org/10.1029/2021JD035872, 2022.

Kanakidou, M., Myriokefalitakis, S., Daskalakis, N., Fanourgakis, G., Nenes, A.,Baker, A. R., K. Tsigaridis, K. and Mihalopoulos ˙N.: Past, Present and Future Atmospheric Nitrogen Deposition, J. Atmos Sci., 73(5): 2039–2047,//doi: 10.1175/JAS-D-15-0278.1 , 2016.

Liu, L., Zhang, X., Wong, A. Y. H., Xu, W., Liu, X., Li, Y., Mi, H., Lu, X., Zhao, L., Wang, Z., Wu, X., and Wei, J.: Estimating global surface ammonia concentrations inferred from satellite retrievals, Atmos. Chem. Phys., 19, 12051–12066, https://doi.org/10.5194/acp-19-12051-2019, 2019.

Kloster, S., Feichter, J., Maier-Reimer, E., Six, K. D., Six, K. D., Steir, P. and Wetzel, P.: DMS cycle in the marine ocean-atmosphere system – a global model study, Biogeosciences, 3, 29-51, https://doi.org/10.5194/bg-3-2006, 2006.

Liu, S., Valks, P., Pinardi, G., Xu, J., Chan, K. L., Argyrouli, A., Lutz, R., Beirle, S., Khorsandi, E., Baier, F., Huijnen, V., Bais, A., Donner, S., Dörner, S., Gratsea, M., Hendrick, F., Karagkiozidis, D., Lange, K., Piters, A. J. M., Remmers, J., Richter, A., Van Roozendael, M., Wagner, T., Wenig, M., and Loyola, D. G.: An improved TROPOMI tropospheric NO_2 research product over Europe, Atmos. Meas. Tech., 14, 7297–7327, https://doi.org/10.5194/amt-14-7297-2021 , 2021.

Liu, S., Geng, G., Xioa, Q., Zheng, Y., Cheng, J.,and Zhang, Q.: Tracking Daily Concentrations of PM2.5 Chemical Composition in China since 2000, Environ. Sci. Technol., 56, 16517-16527, 2022.

Luo, G., Yu, F., and Schwab, J.: Revised treatment of wet scavenging processes dramatically improves GEOS-Chem 12.0.0 simulations of surface nitric acid, nitrate, and ammonium over the United States, *Geosci. Model Dev.*, 12, 3439–3447, https://doi.org/10.5194/gmd-12-3439-2019 , 2019.

Metzger, S., Dentener, F., Pandis, S., and Lelieveld, J.: Gas/aerosol partitioning: 1. A computationally efficient model, J. Geophys. Res., 107, 4312, https://doi.org/10.1029/2001JD001102, 2002.

Metzger, S., Mihalopoulos, N., and Lelieveld, J.: Importance of mineral cations and organics in gas-aerosol partitioning of reactive nitrogen compounds: case study based on MINOS results, Atmos. Chemistry and Physics, 6, 2549–2567, https://doi.org/10.5194/acp-6-2549-2006 , 2006.

Metzger, S., Steil, B., Abdelkader, M., Klingmüller, K., Xu, L., Penner, J. E., Fountoukis, C., Nenes, A., and Lelieveld, J.: Aerosol water parameterisation: a single parameter framework, Atmos. Chem. Phys., 16, 7213–7237, https://doi.org/10.5194/acp-16-7213-2016 , 2016.

Metzger, S., Abdelkader, M., Steil, B., and Klingmüller, K.: Aerosol water parameterization: long-term evaluation and importance for climate studies, Atmos. Chem. Phys., 18, 16747–16774, https://doi.org/10.5194/acp-18-16747-2018, 2018.

Metzger, S., Rémy, S., Williams, J. E., Huijnen, V., and Flemming, J.: A computationally efficient parameterization of aerosol, cloud, and precipitation pH for application at global and regional scale (EQSAM4Clim-v12), Geosci. Model Dev., 17, 5009–5021, https://doi.org/10.5194/gmd-17-5009-2024, 2024.

Myriokefalitakis, S., Bergas-Massó, E., Gonçalves-Ageitos, M., Pérez García-Pando, C., van Noije, T., Le Sager, P., Ito, A., Athanasopoulou, E., Nenes, A., Kanakidou, M., Krol, M. C., and Gerasopoulos, E.: Multiphase processes in the EC-Earth model and their relevance to the atmospheric oxalate, sulfate, and iron cycles, Geosci. Model Dev., 15, 3079–3120, https://doi.org/10.5194/gmd-15-3079-2022, 2022.

Pan, D., Mauzerall, D.L., Wang, R., Guo, X., Puchalski, M., Guo, Y., Song, S., Tong, D., Sullivan, A. P., Schichtel, B. A., Collet Jr, J. L. and Zondlo, M. A.: Regime shift in secondary inorganic aerosol formation and nitrogen deposition in the rural United States. Nat. Geosci. ,https://doi.org/10.1038/s41561-024-01455-9, 2024.

Peuch, V-H., Engelen, R., Rixen, M., Dee, D., Flemming, J., Suttie, M., Ades, M., Agustí-Panareda, A., Ananasso, C., Andersson, E., Armstrong, D., Barré, J., Nicolas Bousserez, N., Dominguez, J. J., Garrigues, S., Inness, A., Jones, L., Kipling, Z., Letertre-Danczak, J., Parrington, M., Razinger, M., Ribas, R., Vermoote, S., Yang, X., Simmons, A., Garcés de Marcilla, J., and Thépaut, J.-N. : The Copernicus Atmosphere Monitoring Service: From Research to Operations, BAMS, E2650–E2668, https://doi.org/10.1175/BAMS-D-21-0314.1, 2024.

Reay, D. S., Dentener, F., Smith, P., Grace, J., and Feely, R. A.: Global nitrogen deposition and carbon sinks, Nat. Geosci., 1, 430–437, 2008.

Rémy, S., Kipling, Z., Flemming, J., Boucher, O., Nabat, P., Michou, M., Bozzo, A., Ades, M., Huijnen, V., Benedetti, A., Engelen, R., Peuch, V.-H., and Morcrette, J.-J.: Description and evaluation of the tropospheric aerosol scheme in the European Centre for Medium-Range Weather Forecasts (ECMWF) Integrated Forecasting System (IFS-AER, cycle 45R1), Geosci. Model Dev., 12, 4627–4659, https://doi.org/10.5194/gmd-12-4627-2019, 2019.

Rémy, S., Kipling, Z., Huijnen, V., Flemming, J., Nabat, P., Michou, M., Ades, M., Engelen, R., and Peuch, V.-H.: Description and evaluation of the tropospheric aerosol scheme in the Integrated Forecasting System (IFS-AER, cycle 47R1) of ECMWF, Geosci. Model Dev., 15, 4881–4912, https://doi.org/10.5194/gmd-15-4881-2022 , 2022.

Renner, E and Wolke, R.: Modelling the formation and atmospheric transport of secondary inorganic aerosols with special attention to regions with high ammonia emissions, Atmos. Environ., 44(15), https://doi.org/10.1016/j.atmosenv.2010.02.018, 2010.

Rémy, S., Metzger, S., Huijnen, V, Williams, J. E. and Flemming, J.: An improved representation of aerosol in the ECMWF IFS-COMPO 49R1 through the integration of EQSAM4Climv12 – a first attempt at simulating aerosol acidity, Geosci. Model Dev., 17, 7539–7567, https://doi.org/10.5194/gmd-17-7539-2024 , 2024.

Seinfeld, J. and Pandis, S.: Atmospheric Chemistry and Physics: From Air Pollution to Climate Change - second edition, New Jersey: John Wiley and Sons, 2006.

Shah, V., Jacob, D. J., Moch, J. M., Wang, X., and Zhai, S.: Global modeling of cloud water acidity, precipitation acidity, and acid inputs to ecosystems, *Atmos. Chem. Phys.*, 20, 12 223–12 245, https://doi.org/10.5194/acp-20-12223-2020, 2020.

Sharma, S. K., Singh, A. K., Saud, T., Mandal, T. K., Saxena, M., Singh, S., Ghosh, S. K., and Raha, S.: Measurement of ambient NH_3 over Bay of Bengal during W_ICARB Campaign, *Ann. Geophys.*, 30, 371–377, https://doi.org/10.5194/angeo-30-371-2012 , 2012.

Sharma, S., Chandra, M., and Kota, S.H.: Health Effects Associated with $PM_{2.5}$: a Systematic Review, *Curr Pollution Rep* **6**, 345–367, https://doi.org/10.1007/s40726-020-00155-3, 2020.

Shephard, M. W., Cady-Pereira, K. E., Luo, M., Henze, D. K., Pinder, R. W., Walker, J. T., Rinsland, C. P., Bash, J. O., Zhu, L., Payne, V. H., and Clarisse, L.: TES ammonia retrieval strategy and global observations of the spatial and seasonal variability of ammonia, Atmos. Chem. Phys., 11, 10743–10763, https://doi.org/10.5194/acp-11-10743-2011, 2011.

Shi, G., Xu, J., Shi, X., Liu, B., Bi, X.,Xiao, Z., et al: Aerosol pH dynamics during haze periods in an urban environment in China: Use of detailed, hourly, speciated observations to study the role of ammonia availability and secondary aerosol formation and urban environment.Journal of Geophysical Research:Atmospheres,124, 9730–9742. https://doi.org/10.1029/2018JD029976, 2019.

Sindelarova, K., Markova, J., Simpson, D., Huszar, P., Karlicky, J., Darras, S., and Granier, C.: High-resolution biogenic global emission inventory for the time period 2000–2019 for air quality modelling, Earth Syst. Sci. Data, 14, 251–270, https://doi.org/10.5194/essd-14-251-2022 , 2022.

Simpson, D, Aas, W., Bartnicki, J., Berge, H., Bleeker, A., Cuvelier, C., Dentener, F., Dore, A. Erisman, J.-W., Fagerli, H., Flechard, C., Hertel, O., Jaarsveld, H., Jenkin, M.E., Schaap, M. Smeena, V.S., Thunis, P., Vautard, R. and Vieno, M.: Atmospheric transport and deposition of reactive nitrogen in Europe. The European Nitrogen Assessment, 298-316, doi:10.1017/CBO9780511976988.017, 2010.

Simpson, R. M. C., S. G. Howell,B. W. Blomquist, A. D. Clarke, and B. J.Huebert, Dimethyl sulfide: Less important than long-range transport as a source of sulfate to the remote tropical Pacific marine boundary layer, J. Geophys. Res. Atmos., 119, 9142–9167, doi:10.1002/2014JD021643, 2014.

Soulie, A., Granier, C., Darras, S., Zilbermann, N., Doumbia, T., Guevara, M., Jalkanen, J.-P., Keita, S., Liousse, C., Crippa, M., Guizzardi, D., Hoesly, R., and Smith, S.: Global Anthropogenic Emissions (CAMS-GLOB-ANT) for the Copernicus Atmosphere Monitoring Service Simulations of Air Quality Forecasts and Reanalyses, Earth Syst. Sci. Data, 16, 2261–2279, https://doi.org/10.5194/essd-16-2261-2024 , 2024.

Sun, Y., Guo, G., Li, Y., Luo, G., Li, L., Yuan, H., Mur, L. A. J. and Guo, S.: Negative effects of the simulated nitrogen deposition on plant phenolic metabolism: A meta-analysis, *Sci. Total Environ.,* 19, 137–142, 2020.

Tan, J., Fu, J. S., Dentener, F., Sun, J., Emmons, L., Tilmes, S., Sudo, K., Flemming, J., Jonson, J. E., Gravel, S., Bian, H., Davila, Y., Henze, D. K., Lund, M. T., Kucsera, T., Takemura, T., and Keating, T.: Multi-model study of HTAP II on sulphur and nitrogen deposition, *Atmos. Chem. Phys.*, 18, 6847–6866, https://doi.org/10.5194/acp-18-6847-2018 , 2018.

Tang, Y. S., Flechard, C. R., Dämmgen, U., Vidic, S., Djuricic, V., Mitosinkova, M., Uggerud, H. T., Sanz, M. J., Simmons, I., Dragosits, U., Nemitz, E., Twigg, M., van Dijk, N., Fauvel, Y., Sanz, F., Ferm, M., Perrino, C., Catrambone, M., Leaver, D., Braban, C. F., Cape, J. N., Heal, M. R., and Sutton, M. A.: Pan-European rural monitoring network shows dominance of NH_3 gas and NH_4NO_3 aerosol in inorganic atmospheric pollution load, Atmos. Chem. Phys., 21, 875–914, https://doi.org/10.5194/acp-21-875-2021 , 2021.

Tichý, O., Eckhardt, S., Balkanski, Y., Hauglustaine, D., and Evangeliou, N.: Decreasing trends of ammonia emissions over Europe seen from remote sensing and inverse modelling, Atmos. Chem. Phys., 23, 15235–15252, https://doi.org/10.5194/acp-23-15235-2023, 2023.

Tørseth, K., Aas, W., Breivik, K., Fjæraa, A. M., Fiebig, M., Hjellbrekke, A. G., Lund Myhre, C., Solberg, S., and Yttri, K. E.: Introduction to the European Monitoring and Evaluation Programme (EMEP) and observed atmospheric composition change during 1972–2009, Atmos. Chem. Phys., 12, 5447–5481, https://doi.org/10.5194/acp-12-5447-2012, 2012.

Turnock, S. T., Mann, G. W.,Woodhouse, M. T., Dalvi, M.,O'Connor, F. M., Carslaw, K. S., and Spracklen, D. V.: The impact of changes in cloud water pH on aerosol radiative forcing, Geophys. Res. Lett., 46, 4039–4048. https://doi.org/10.1029/2019GL082067, 2019.

Ting. Y.C., Young, L.H., Lin TH, Tsay, S.C., Chang, K.E. and Hsiao, T.C: Quantifying the impacts of $PM_{2.5}$ constituents and relative humidity on visibility impairment in a suburban area of eastern Asia using long-term in-situ measurements. Sci Total Environ. 2022 Apr 20;818:151759. doi: 10.1016/j.scitotenv.2021.151759. Epub 2021 Nov 22. PMID: 34822889, 2022.

Tørseth, K., Aas, W., Breivik, K., Fjaeraa, A. M., Fiebig, M., Hjellbrekke, A. G., Lund-Myrhe, C., Solberg, S. and Yttri, K. E.: Introduction to the European Monitoring and Evaluation Programme (EMEP) and observed atmospheric composition change during 1972–2009, Atmos. Chem. Phys., 12, pp. 5447-5481, 2012.

van Noije, T. P. C., Le Sager, P., Segers, A. J., van Velthoven, P. F. J., Krol, M. C., Hazeleger, W., Williams, A. G., and Chambers, S. D.: Simulation of tropospheric chemistry and aerosols with the climate model EC-Earth, Geosci. Model Dev., 7, 2435–2475, https://doi.org/10.5194/gmd-7-2435-2014, 2014.

Verheggen, B., Cozic, J., Weingartner, E., Bower, K., Mertes, S., Connolly, P., Gallagher, M., Flynn, M., Choularton, T., and Baltensperger, U.: Aerosol partitioning between the interstitial and the condensed phase in mixed-phase clouds, Journal of Geophysical Research: Atmospheres, 112, https://doi.org/https://doi.org/10.1029/2007JD008714, 2007.

Verstraeten, W. W., Boersma, K. F. , Douros, J., Williams, J. E., Eskes, H., Liu, F., Beirle, S. and Delcloo, A.: Top-Down NOX Emissions of European Cities Based on the Downwind Plume of Modelled and Space-Borne Tropospheric NO2 Columns, Sensors, 18, 2893, http://dx.doi.org/10.3390/s18092893, 2018.

Vestreng, V., Myhre, G., Fagerli, H., Reis, S., and Tarrasón, L.: Twenty-five years of continuous sulphur dioxide emission reduction in Europe, Atmos. Chem. Phys., 7, 3663–3681, https://doi.org/10.5194/acp-7-3663-2007, 2007.

Vieno, M., Heal, M. R., Hallsworth, S., Famulari, D., Doherty, R. M., Dore, A. J., Tang, Y. S., Braban, C. F., Leaver, D., Sutton, M. A., and Reis, S.: The role of long-range transport and domestic emissions in determining atmospheric secondary inorganic particle concentrations across the UK, Atmos. Chem. Phys., 14, 8435–8447, https://doi.org/10.5194/acp-14-8435-2014 , 2014.

Vinken, G. C. M., Boersma, K. F., Jacob, D. J., & Meijer, E. W.: Accounting for non-linear chemistry of ship plumes in the GEOS-Chem global chemistry transport model. Atmospheric Chemistry and Physics, 11(22), 11707-11722. https://doi.org/10.5194/acp-11-11707-2011, 2011.

Wang, J., Xu, J., He, Y., Chen, Y., and Meng, F.: Long range transport of nitrate in the low atmosphere over Northeast Asia, Atmos. Environ., 144, 315-324, https://doi.org/10.1016/j.atmosenv.2016.08.084, 2016.

Wang, R., Pan, D., Guo, X., Sun, K., Clarisse, L., Van Damme, M., Coheur, P.-F., Clerbaux, C., Puchalski, M., and Zondlo, M. A.: Bridging the spatial gaps of the Ammonia Monitoring Network using satellite ammonia measurements, Atmos. Chem. Phys., 23, 13217–13234, https://doi.org/10.5194/acp-23-13217-2023 , 2023.

Williams., J. E., van der Swaluw, E., de Vries, W. J., Sauter, F. J., van Pul, W.A.J. and Hoogerbrugge, R.: Modelling the future distribution of ammonium nitrate concentrations in The Netherlands for 2020: The sensitivity to meteorological parameters, Atmos. Environm., Volume: 115, 278-285, doi: 10.1016/j.atmosenv.2015.06.001, 2015.

Williams, J. E ., Huijnen, V., Bouarar, I., Meziane, M., Schreurs, T., Pelletier, S., Marécal, V., Josse, B., and Flemming, J.: Regional evaluation of the performance of the global CAMS chemical modeling system over the United States (IFS cycle 47R1), Geosci. Model Dev., 15, 4657–4687, https://doi.org/10.5194/gmd-15-4657-2022 , 2022.

1203 Zhang, L., Jacob, D. J., Knipping, E. M., Kumar, N., Munger, J. W., Carouge, C. C., van Donkelaar, A., Wang, Y.
1204 X., and Chen, D.: Nitrogen deposition to the United States: distribution, sources, and processes, Atmos. Chem.
1205 Phys., 12, 4539–4554, https://doi.org/10.5194/acp-12-4539-2012, 2012.

1206

1207